Artifacts in high-frequency passive surface wave dispersion imaging – Towards the linear receiver array

Feng Cheng[1,*], Jianghai Xia[1], and Chaoqiang Xi[2]

[1]Key Laboratory of Geoscience Big Data and Deep Resource of Zhejiang Province; School of Earth Sciences, Zhejiang University, 866 Yuhangtang Road, Hangzhou 310058, Zhejiang, China
[2]State Key Laboratory of Mining Response and Disaster Prevention and Control in Deep Coal Mines; School of Earth and Environment, Anhui University of Science and Technology, Huainan 232001, Anhui, China
[*]To whom correspondence should be addressed; E-mail: fengcheng@zju.edu.cn.

Article Highlights

- Passive source surface wave methods, including data processing workflow and dispersion image scheme, are reviewed;
- Two general groups of artifacts, that were frequently observed in dispersion imaging but poorly understand in the past, are summarized;
- Solutions and guidelines are provided to avoid and/or attenuate the artifacts before and after field observations.

Abstract

Passive surface wave methods are non-invasive, low-cost, and robust approaches to image near-surface shear-wave velocity (Vs) structure using passive seismic sources, like traffic noises. A clean and high-resolution dispersion image is critical for surface wave analysis. In practice, however, artifacts or aliasing are almost inevitable in passive surface wave dispersion measurements, and seriously pollute the measured dispersion spectra. It is significant to clarify how they are generated, how they affect the dispersion measurement, and how they can be attenuated. We provide the first comprehensive review on artifacts that are frequently observed in high-frequency (>1 Hz) passive surface wave dispersion measurements, and summarize them into two general groups: geometry-related artifacts and source-related artifacts. Mathematical derivations and numerical as well as field examples are presented to explain underlying physics of various artifacts and explore potential solutions and guidelines to attenuate them before and after field observations. This work will help the reader understand the complexity of the measured dispersion spectra, and lead to improvements on rapidly advancing passive surface wave methods.

Keywords: High frequency, Surface wave analysis, Passive source, Dispersion measurement, Artifacts, Geometry, Noise source distribution

1 Introduction

Surface waves are guided and dispersive. Shear-wave velocity (Vs) structure can be determined by inverting the dispersive phase velocity of surface waves (Dorman and Ewing, 1962), due to the high sensitivity of dispersion curves to S-wave velocity (Xia et al., 1999). With advantages of cost, acquisition time, and robustness, surface wave methods, particularly techniques based on analysis of Rayleigh waves, have been widely utilized at multiple scales in both engineering and geological studies (Miller et al., 1999; Xia et al., 1999, 2009; Socco et al., 2010; Nakata et al., 2011; Foti et al., 2014, 2018). They can be classified into two groups associated with the energy source type: active-source surface wave methods and passive-source surface wave methods. Active-source surface wave methods usually use sledgehammers (Park et al., 1998), weight drops (Xia et al., 2000), or vibrators (Miller et al., 1999) as seismic sources. The passive-source surface wave methods use ambient seismic energy from natural or anthropogenic sources (e.g., small earthquakes (Poupinet et al., 1984), ocean-seafloor interaction (Lepore and Grad, 2020), traffic (Nakata et al., 2011), and industrial activities (Pan et al., 2016)).

Passive-source surface wave methods have flourished over the past two decades in the geophysical and civil engineering communities because of the logistical challenges and costs from traditional seismic surveys, particularly in highly populated urban areas. The first passive-source surface wave study originated over 60 years ago in pioneering works by Aki (1957, 1965), which is known as the spatial autocorrelation (SPAC) method. Okada and Suto (2003) offers a comprehensive review of the SPAC method and further extended the SPAC method using microtremor array measurement (MAM) to improve the flexibility of the receiver configuration and the investigation depth of the objective structure. Under the considering of 2D array, for example dense nodal array, SPAC method is flexible for various geometry configurations (Asten and Hayashi, 2018; Cho and Iwata, 2021) and can be extended to multicomponent recordings (Haney et al., 2012). Studies and applications also prove that SPAC method works for the linear array (Chávez-García et al., 2006; Margaryan et al., 2009; Kita et al., 2011), rather than the traditional SPAC (Aki, 1957) using a circle array or the two-station SPAC (Ekström et al., 2009; Hayashi et al., 2013), although they all share the same mathematical base of fitting the Bessel function (the function itself or the zero-crossing of the function) with the spatial autocorrelation coefficient. Recently, a similar technique, the frequency-Bessel (F-J) transform, attracts broad attentions from seismology and engineering communities due to the ability to improve higher modes with an appropriate spectral decomposition on the frequency-Bessel spectrogram (Forbriger, 2003; Wang et al., 2019; Hu et al., 2020; Wu et al., 2020; Xi et al., 2021).

Aki's work has been revisited in light of advances of ambient noise interferometry technique following the groundbreaking work of Campillo and Paul (2003). Ambient noise interferometry estimates Green's functions between cross-correlation of two receivers from the ambient seismic field (Shapiro and Campillo, 2004; Snieder, 2004; Wapenaar, 2004; Bensen et al., 2007; Snieder et al., 2009; Nakata et al., 2015; Paitz et al., 2019; Tsai and Sager, 2022). This approach has been applied to characterize multiple scales of earth structure: from global or continental scale deep-structure imaging in seismology (e.g., Yang et al., 2007; Lin et al., 2008; Yao and van der Hilst, 2009; Lin et al., 2009; Strobbia and Cassiani, 2011; Tibuleac and von Seggern, 2012; Becker and Knapmeyer-Endrun, 2018; Chen et al., 2021; Xu et al., 2022) to local scale exploration (e.g., Bakulin and Calvert, 2006; Wapenaar et al., 2008; Draganov et al., 2009; Nakata et al., 2011; Ali et al., 2013; Behm et al., 2014; Nakata et al., 2016; Behm et al., 2016; Castellanos et al., 2020; Cheng et al., 2021b). During the last decade, ambient noise interferometry has also found a variety of applications in the near-surface characterization domain (e.g., Foti et al., 2011; O'Connell and Turner, 2011; Xu et al., 2013; Cheng et al., 2015; Shirzad et al., 2015; Foti et al., 2018; Dou et al., 2017; Cheng et al., 2018a; Cárdenas-Soto et al., 2021; Fu et al., 2022). Considering ambient noise interferometry technique turns the physical receivers into virtual sources, it offers the potential to apply active-source seismic methods on passive-source seismic data. Cheng et al. (2016) provide a method by combining ambient noise interferometry and multichannel analysis of surface wave for passive-source surface wave dispersion imaging, called multichannel analysis of passive surface waves (MAPS). Recent applications have proven the rationality and effectivity of the MAPS method on near-surface structure investigations (Zhou et al., 2018; Pang et al., 2019; Liu et al., 2020; Dai et al., 2021; Mi et al., 2022; Chen et al., 2022).

Apart from the interferometry-based methods, several passive-source surface wave approaches have already existed and been popular in the seismic engineering communities in the early 2000s. Louie (2001) presented the refraction microtremor (ReMi) method as a fast and effective passive-source surface wave imaging method based on the $\tau - p$ transformation, or slant-stacking (Thorson and Claerbout, 1985). Park et al. (2004) introduced a similar strategy for dispersion imaging of passive-source surface waves using the phase-shift method, called passive multichannel analysis of surface wave (PMASW). Besides, two-dimensional (2D) array based method, frequency-wavenumber (f-k) analysis (Capon, 1969; Lacoss et al., 1969), has also been revisited and extended for 1D linear array application (Liu et al., 2020). Due to their simplicity and effectiveness, these linear array based passive surface wave methods have been widely utilized for basin-scale shear-velocity structure mapping, earthquake hazard class assessment as well as infrastructure seismic site classification (Stephenson et al., 2005; Pancha et al., 2008; Louie et al., 2011; Pancha et al., 2017; Bajaj and Anbazhagan, 2019; Louie et al., 2021; Asten et al., 2022; Hayashi et al., 2022).

Based on the data processing schemes, the above mentioned passive-source surface wave methods can be roughly divided into two groups: non-interferometric methods (e.g., ReMi and PMASW) and interferometric methods (e.g., MAPS and SPAC). Non-interferometric methods directly extract dispersion measurements from ambient seismic records (Louie, 2001; Park et al., 2004), while interferometric methods calculate interferograms before dispersion measurements is applied, where interferograms are either empirical Green's function (Cheng et al., 2016) or spatial autocorrelation coefficients (also known as spatially averaged coherency (Asten, 2006; Chávez-García et al., 2006)). Several studies have explicitly provided the equivalent relationship between Green's functions (or cross-correlation functions) and spatial autocorrelation functions (Asten, 2006; Nakahara, 2006; Tsai and Moschetti, 2010; Haney et al., 2012). However, recent works have argued that interferometric methods are superior to non-interferometric methods (Cheng et al., 2016; Xu et al., 2017). Cheng et al. (2020) provided comprehensive comparisons between non-interferometric and interferometric passive-source surface wave imaging methods, and concluded that the interferometric methods usually offer more accurate dispersion imaging in terms of the linear acquisition system, while the non-interferometric methods have the potential advantage to highlight the trend of the fundamental mode dispersion energy.

Regardless of the source types, a clean and high-resolution dispersion image without artifacts is critical for surface wave analysis including dispersion curve picking and the subsequent Vs inversion. Lots of studies have attempted to improve active-source surface wave dispersion measurements, for example, attenuating the near-field and far-field effects (Zywicki and Rix, 2005; Park and Carnevale, 2010; Roy and Jakka, 2017; Foti et al., 2018), enhancing dispersion imaging resolution (Luo et al., 2008; Mikesell et al., 2017), deblurring of surface wave dispersion spectra (Picozzi et al., 2010; Cheng et al., 2021c), analyzing and filtering surface wave energy (Park et al., 2002; Ivanov et al., 2005). In spite of the truth that passive-source surface wave methods usually provides much worse dispersion measurements and artifacts are almost inevitable, however, few literatures were devoted to investigate why artifacts exist on passive surface wave dispersion spectra, and how to attenuate them. Turner (1990) presented the aliasing problems in the $\tau - p$ transform due to the insufficient spatial sampling. Cheng et al. (2018b) first discussed a kind of "crossed" artifacts for high-frequency passive-source surface wave surveys, explaining the underlying physics and proposed an effective way to attenuate them by using FK-based data selection. Dai et al. (2018) discussed the effects of aliasing on wavefield decomposition.

In this work, we seek to provide a comprehensive review on artifacts that are frequently observed in surface wave dispersion measurements, and explore how they are generated and how to eliminate them. The current paper is organized as follows. We first briefly review the frequently-used passive surface wave methods, including their data processing workflow and the mathematical derivations of the dispersion imaging scheme. Next, we summarize two groups of artifacts resulted from inappropriate geometry configuration and non-uniform noise source distribution, respectively. Both numerical and field examples, as well as mathematical derivations, are presented to help the reader understand sources of various types artifacts and solutions to attenuate them. We also discuss artifacts from the non-interferometric methods which usually produce biased dispersion information. Finally, we present a brief conclusion, as well as some guidelines, for passive-source surface wave survey and dispersion imaging.

In this paper, we use terminology "high-frequency surface wave" to limit the scope of this work to near surface scale including passive-source surface wave surveys with frequency band above 1 Hz as well as active-source surface wave surveys with frequency band above 10 Hz. The frequency band ($>$ 1 Hz) is relatively higher compared to the long period ($>$ 30 s) for teleseismic surface waves used in global scale ambient noise applications. We focus on high-frequency surface waves because they contribute significantly to urban seismic noise in a broad frequency range from 1 Hz to more than 45 Hz with maximum amplitudes between 1 and 10 Hz (Groos and Ritter, 2009). Besides, it is worth noting that this work focuses on the linear receiver array, which is often deployed for both passive-source and active-source surface wave investigations because of its high efficiency and convenience. In populated urban areas, it is challenging to construct dense 2-D arrays due to the spatial restrictions imposed by existing infrastructures. Linear receiver arrays are a natural geometry for road-side investigations utilizing receivers deployed on shoulders or median strip areas. Linear array techniques are also useful when processing distributed acoustic sensing (DAS) data, a recently developed technique which utilizes subsurface fiber-optic cables to capture earth vibrations for seismic imaging (Dou et al., 2017; Ajo-Franklin et al., 2019; Zhan, 2020; Cheng et al., 2021a, 2022).

2 Passive surface wave methods

2.1 Passive surface waves data processing

The key difference between the active-source and passive-source surface wave methods is that the latter requires sufficient temporal and/or spectral ensemble averaging/stacking to enhance the coherent signals as well as cancel the incoherent noises from the inhomogeneous noise source distribution. Figure 1 presents the basic data processing schemes for two types of passive-source surface wave methods: the non-interferometric methods (e.g., ReMi (Louie, 2001) and PMASW (Park et al., 2004)), and the interferometric methods (e.g., MAPS (Cheng et al., 2016) and SPAC (Chávez-García et al., 2006)).

The data processing workflow before dispersion curve picking and inversion is made up of four steps.

(1) Observing the continuous and long-duration ambient noise records. In general, several tens of minutes duration is sufficient for urban passive-source surface wave survey (Cheng et al., 2018b; Foti et al., 2018; Vantassel and Cox, 2022).
(2) Splitting the continuous time series into short overlapped time segments. According to our experiences, a 10s window with a 75% overlap is a good trade-off between efficiency and signal quality (Cheng et al., 2018b; Foti et al., 2018).
(3) Preprocessing short time segments to remove potential near-field interferences and extend frequency bandwidth. The basic data preprocessing workflow includes tapering two ends, removing the mean, the linear trend, the dead traces, as well as the instrument response as necessary, temporal normalization, and spectral whitening, for each individual time segment (Bensen et al., 2007; Cheng et al., 2018b).
(4) Estimating dispersion spectra with an appropriate approach. Dispersion measurement or imaging is the vital step for surface wave analysis. Slant-stacking algorithm has been primarily used as an array-based data processing approach to extract phase velocity dispersion information for both land seismic survey (e.g., Xia et al., 2009) and marine seismic survey (e.g., Bohlen et al., 2004).

As shown on Figure 1, differences exist between non-interferometric and interferometric methods for dispersion imaging. For example, non-interferometric methods (e.g., PMASW and ReMi) directly measure individual dispersion spectra from each preprocessed short time segments and spectrally stack all dispersion spectra together to obtain the final enhanced dispersion spectra; while interferometric methods (e.g., MAPS and SPAC) implement a single dispersion measurement on the final temporally stacked interferograms. Here we provide a brief introduction on the dispersion image scheme for both methods.

2.2 Passive surface wave dispersion analysis

Several recent studies have presented reviews between non-interferometric methods and interferometric methods and indicated the similarity as well as the uniqueness of their dispersion imaging schemes (Xu et al., 2017; Cheng et al., 2018b, 2020; Ning et al., 2022). For simplicity, we only focus on the PMASW and MAPS method to introduce the mathematical background of passive surface wave dispersion imaging.

2.2.1 The non-interferometric method, PMASW

The PMASW method employs a slant-stacking algorithm to transfers the wavefield from the offset-time ($x - t$) domain to the frequency-velocity ($f - v$) domain (Park et al., 1998, 2004) domain. In order to account for the universally bidirectional characteristic of the observed passive surface waves, both the forward propagating waves with positive velocity ($+v$) and the backward propagating waves with negative velocities ($-v$) are scanned in the slant-stacking procedure.

Under the in-line source distribution environment, we follow Cheng et al. (2018b) to present the obtain dispersion spectra in frequency-wavenumber ($f-k$) domain as

$$E(f,k) = |e^{\phi_0}| * \left(\left| \sum_{j=1}^{N} e^{i2\pi[k(f)-k_0(f)]x_j} \right| + \left| \sum_{j=1}^{N} e^{-i2\pi[k(f)+k_0(f)]x_j} \right| \right) \quad (1)$$

where, $E(f,k)$ is the measured dispersion spectra; ϕ_0 is the initial phase term; k_0 is wavenumber which is associated with the target dispersion curve by the relationship of $k = f/v$; x_j denotes the offset; $j \in (1..N)$. Eq.1 explains how the PMASW method estimates the dispersion information. Note that this equation only holds under the perfect in-line source distribution assumption, and the biased artifacts in non-interferometric dispersion measurements will be further discussed later.

2.2.2 The interferometric method, MAPS

To enhance the coherent signals among the ambient noise, Cheng et al. (2016) proposed a hybrid method, MAPS, that applies cross-correlations, rather than raw noise records, to PMASW. Under the in-line source distribution environment, we follow conventions in Cheng et al. (2020) to present the cross-correlation spectrum C_{x_1,x_2} as

$$\begin{aligned} C_{x_1,x_2} &= u(x_1,\omega)u^*(x_2,\omega) \\ &= \sum_{j=1}^{N_s} [e^{-i2\pi k_0(w)x_1} e^{i2\pi k_0(w)x_2}] + \overline{C_{x_1,x_2}}, \end{aligned} \quad (2)$$

where, $\overline{C_{x_1,x_2}}$ is the cross term; ω is the angle frequency; N_s is the total source number; $u(x_1,\omega)$ and $u(x_2,\omega)$ indicate the ambient noise spectral wavefield following the representation $u(x,\omega) = \sum_{j=1}^{N_s} e^{i(\omega t_{s_i} - 2\pi k_0 r_{s_i} - 2\pi k_0 x)}$ (eq.2 in Cheng et al. (2020)) considering an in-line source distribution case.

Because noise sources are assumed to be uncorrelated in time and space, and the contribution of each source to the cross-correlation function could be determined independently (Tromp et al., 2010; Lawrence et al., 2013), the cross term $\overline{C_{x_1,x_2}}$ is negligible given a sufficiently time-averaged ensemble. Applying the ensemble averaging along the time direction yields the ensemble averaged cross-correlation spectrum $\langle C_{x_1,x_2} \rangle$ under the in-line source distribution

$$\begin{aligned} \langle C_{x_1,x_2} \rangle &= \langle \sum_{j=1}^{N_s} [e^{-i2\pi k_0(w)x_1} e^{i2\pi k_0(w)x_2}] + \overline{C_{x_1,x_2}} \rangle \\ &\approxeq e^{-i2\pi k_0(w)x_{1,2}}, \end{aligned} \quad (3)$$

where, $\langle ... \rangle$ indicates the ensemble averaging. To obtain the MAPS representation, we employ the slant-stacking algorithm on the phase term of the ensemble averaged cross-correlation spectrum

$$\begin{aligned} E(f,k) &= |\sum_{m=1}^{N-1}\sum_{n=m+1}^{N} e^{i2\pi k(f)x_{m,n}} \frac{\langle C_{x_m,x_n}\rangle}{|\langle C_{x_m,x_n}\rangle|}| \\ &= |\sum_{m=1}^{N-1}\sum_{n=m+1}^{N} e^{i2\pi[k(f)-k_0(f)]x_{m,n}}|, \end{aligned} \quad (4)$$

where, $\sum_{m=1}^{N-1}\sum_{n=m+1}^{N}$ denotes the C_N^2 inter-station cross-correlation pairs summation of MAPS, comparing to the C_N^1 channel number summation of MASW. The energy peaks of $E(f,k)$ will occur where the scanning wavenumber (k) approaches the true wavenumber (k_0) of the coherent signal. Eq.4 demonstrates the ability of interferometric methods to produce the accurate dispersion curve once we are confident of the retrieved signals from virtual sources (e.g., empirical Green's function or spatially averaged coherency).

3 Artifacts in passive surface wave dispersion imaging

Compared with the active-source methods, the passive-source surface wave methods have the advantage of extending the dispersion measurement to lower frequencies, but suffer from incoherent noise, particularly at higher frequencies, due to the unknown distribution of ambient noise sources (Cheng et al., 2018b, 2019). In this study, we summarize these frequently observed imaging artifacts into two groups: the geometry-related artifacts and the source-related artifacts, and explore their underlying physics according to above numerical derivations. Details about their characteristics as well as solutions to attenuate them will be expanded.

3.1 The geometry-related artifacts

Array geometry configuration is vital for seismic acquisitions. Given an array with limited receiver numbers, people have to enlarge spatial interval (dx) to increase spatial coverage for observation of signals with longer wavelengths which are required for deeper depth exploration. In addition, people also have to trade off the exploration depth and the lateral resolution in terms of array length (L) design, because the deeper exploration depth prefers longer array length while the finer lateral resolution expects shorter array length to limit spatial average. Therefore, array geometry affects the passive surface wave dispersion measurements, and might produce various of artifacts in case of the sparse spatial sampling or the insufficient array coverage.

3.1.1 Artifacts from spare spatial sampling, large dx

Based on the derivations for the surface wave dispersion measurement (eq.1 for the PMASW method and eq.4 for the MAPS method), the energy peaks of $E(f, k)$ will occur when the scanning wavenumber k approaches the true dispersion curve k_0 of the coherent signal. However, previous studies (Cheng et al., 2018b; Dai et al., 2018) imply that $k = k_0$ might not be the unique solution. Considering the similarity between eq.1 and eq.4, here, we focus on the latter to explore solutions of the dispersion spectra equation.

Given an evenly sampled acquisition system, which is commonly used in shallow-structure surface wave survey, we define $x_{m,n} = (m-n) * dx$ for simplicity. Based on Euler formula, we expand eq.4 as

$$
\begin{aligned}
E(f,k) &= \left| \sum_{m=1}^{N-1} \sum_{n=m+1}^{N} e^{i2\pi[k(f)-k_0(f)]x_{m,n}} \right| \\
&= \left| \sum_{m=1}^{N-1} \sum_{n=m+1}^{N} cos\{2\pi[k(f)-k_0(f)]x_{m,n}\} + i * sin\{2\pi[k(f)-k_0(f)]x_{m,n}\} \right| \\
&= \left| \sum_{m=1}^{N-1} \sum_{n=m+1}^{N} cos\{2\pi[m-n][k(f)-k_0(f)]dx\} + i * sin\{2\pi[m-n][k(f)-k_0(f)]dx\} \right| .
\end{aligned} \tag{5}
$$

According to the periodicity of the trigonometric function, k_0 is indeed not the unique solution of eq.5 or eq.4. We list four generalized solutions as follows:

$$k(f) = k_0(f) - \frac{j}{dx},\ (k_0(f) > 0) \tag{6a}$$

$$k(f) = k_0(f) + \frac{j}{dx},\ (k_0(f) > 0) \tag{6b}$$

$$k(f) = -k_0(f) + \frac{j}{dx},\ (k_0(f) < 0) \tag{6c}$$

$$k(f) = \frac{j}{dx},\ (k_0(f) \ll dx) \tag{6d}$$

where, j denotes an non-negative integer. Given a sufficient large dx, the aliasing solutions of k in eq.6 would possess a high possibility to be visible at measured dispersion energy window with wavenumber around the real k_0. Eq.6 presents the underlying physics of four types of spatial aliasing dispersion energy that could be observed on passive surface wave measurements, considering their relatively sparse geometry in real-world applications.

Spatial aliasing is artifact due to undersampling, and is usually related to the higher frequencies considering their shorter wavelengths. Several studies have been carried out to understand spatial aliasing (Turner, 1990; Li et al., 1991; Rafaely et al., 2007; Yan et al., 2016; Dai et al., 2018). Note that, the spatial aliasing is not a serious issue for active-source surface wave surveys due to their dense sampling acquisitions; but possibilities still exist depending on the measured frequency range and the sampling distance. Figure 2 illustrates the different characteristics of four types of spatial aliasing, A, B C and D, in terms of two spatial intervals, $dx = 2m$ (Fig.2a) and $dx = 10m$ (Fig.2b).

Spatial aliasing artifacts: type A and type B

According to eq.6a, the type A spatial aliasing is less likely to be visible on the low velocity surface wave target window, because its smaller wavenumber value, compared to k_0, indicates the higher velocity value at a specific frequency. However, cautions still should be paid since it might be recognized as higher modes of surface waves and cause mode misidentification in surface wave inversion (Dai et al., 2018).

In contrast, the type B spatial aliasing (eq.6b) is quite common in passive surface wave dispersion measurements (Foti et al., 2018). It appears as a series of lower velocities energy as predicted by the blue triangles in Figure 2, and will not interfere the true dispersion energy trend since it usually lies below the dispersion energy trend in the $f - v$ domain. It is seldom to observe both types of spatial aliasing on the same passive surface wave dispersion image. Figure3 presents a typical oil-field example with both type of artifacts existing on the dispersion spectra.

Spatial aliasing artifacts: type C

According to eq.6c, the type C spatial aliasing will occur when $k_0 < 0$. It indicates the slant-stacking algorithm is scanning a reverse (backward) propagating surface wave train instead of the expected forward propagating one ($k_0 > 0$). Also, eq.6c is consistent with the finding of Cheng et al. (2018b), which demonstrated the existence of a type of "crossed" artifacts due to the bidirectional velocity scanning scheme in non-interferometric passive-source surface wave methods. It usually occurs on the dispersion measurements of non-interferometric passive surface wave methods, which technically sum the dispersion spectra from both the forward and the reverse directions to account for the possible bidirectional nature of the recorded passive surface waves (Louie, 2001; Park et al., 2004; Xu et al., 2017; Cheng et al., 2018b). Whereas, the ambiguity of the propagation direction of the incoming surface waves produces the "crossed" artifacts in non-interferometric dispersion measurement, which is exactly the type C spatial aliasing artifacts discussed in this work.

We present a field example of passive-source surface wave survey to show the type C spatial aliasing (Fig.4). The data contain 10-min traffic noise records with a 24 vertical-component receiver array. The spatial interval is 10 m. The dataset was first reported by Cheng et al. (2018b). We observe clear "crossed" artifacts on the PMASW dispersion spectra (Fig.4a1) due to its bidirectional slant-stacking scheme; while the MAPS method produces a clean dispersion image (Fig.4b1) because the direction of the scanning velocity has been defined as from virtual sources to virtual receivers. Besides, we can also observe "crossed" artifacts on the raw SPAC measurement (Fig.4c1), which is a special case since the slant-stacking scheme does not apply here. Instead, it is associated with the systematic bias of SPAC and directional aliasing (Cho et al., 2008). Based on eq.6c, we are also able to predict these spatial aliasing artifacts by using the picked multi-mode dispersion curves from MAPS measurement. The predicated type C spatial aliasing generally fits the "crossed" artifacts (the black dots on Figs.4a1 and c1), although distortions exist due to the picking biases. Besides, the predicted type B spatial aliasing (the blue triangles on Fig.4) also matches the linear artifacts at the bottom right of the spectra window.

It is obvious that the "crossed" artifacts seriously smear the dispersion energy, particularly at the higher frequency band and the higher overtones. To attenuate this type of aliasing, we follow Cheng et al. (2018b) to automatically detect the dominant propagating direction of the ambient noise wavefield in $f-k$ domain for each segment to avoid the summation of the opposite dispersion energy. Figure 4a2 shows the improved PMASW measurement with "crossed" artifacts significantly attenuated. Considering the periodicity and symmetry characteristic of Bessel function or Hankel function (Forbriger, 2003; Cho et al., 2008), we also successfully attenuate these artifacts on SPAC measurement (Fig.4c2) by replacing the Bessel function used in SPAC fitting with the adaptive Hankel functions (Xi et al., 2021).

Spatial aliasing artifacts: type D

According to eq.6d, the type D spatial aliasing is independent of the true dispersion energy (no k_0 involved in the equation), and presents as a series of linear strips on the $f-v$ domain (or a series of paralleled horizontal lines on the $f-k$ domain). We provide a dataset with large spatial distance (1 km) as an example of the type D spatial aliasing. The dataset consists of 16 days ambient noise data recorded by 35 broadband seismometers (Trillium 120 P/PA), which has been reported by Xu et al. (2016) and Pan et al. (2016). We apply ambient noise interferometry (cross-coherence) to retrieve the coherent Rayleigh waves from the vertical component. We stack over all the inter-station pairs of empirical Green's functions into discrete 1 km offset bins (Fig.5a) to further enhance the retrieved coherent signals. The linear artifacts that cross the fundamental dispersion energy are distinct on Figure5b), and they can be distinguished as the type D spatial aliasing using the predicted aliasing (the green dashed line) based on eq.6d.

Since the type D spatial aliasing presents as linear artifacts with constant wavenumber, it can be easily attenuated in $f-k$ domain using filter techniques, for example, the median filter (Duncan and Beresford, 1995) and the FK filter (Zhou, 2014). Figure 5c displays an example of aliasing attenuation using the FK filter. The filtered dispersion spectra has been improved with extended frequency bandwidth and attenuated distortions at low frequencies, although some weak linear aliasing artifacts still exist at high frequency due to the leakage of the FK filter.

3.1.2 Artifacts from insufficient array coverage, short L

The spatial interval (dx) controls the maximum wavenumber (k_{max}) sampled with the array, whereas, the length of the array (L) determines the minimum resolvable wavenumber ($k_{min} = 1/L$). k_{min} can be taken as the absolute wavenumber resolution according to the Fourier analysis theory (Stein and Shakarchi, 2011) or the imaging resolution of the surface wave dispersion spectra (Johnson and Dudgeon, 1993). Besides, k_{min} also controls the bottom frequency boundary of the dispersion measurement since the minimum wavenumber is linearly associated with the lowest frequency.

We carry out two similar numerical tests based on linear arrays with different array lengths, 100 m and 20 m, to generate 15-min ambient noise records with the same random distributed source configuration as indicated in Figure 6. We then apply the MAPS method for dispersion imaging. Note that no data preprocessing operator is included prior to noise cross-correlation to avoid potential influences from the preprocessing operators, like spectra whitening, on the frequency bandwidth of the measured dispersion spectra. We observe that the measured dispersion spectra fits the theoretical dispersion curve well for both array when the scanning wavenumber k is above the minimum resolvable wavenumber k_{min} (the blue dashed line). However, when the scanning wavenumber goes beyond the absolution resolution of wavenumber $k < k_{min}$, the dispersion energy turns to be biased. Therefore, we usually employ k_{min} as an approximate quality control indicator to avoid artifacts at low frequency due to array aperture. It is worth noticing that k_{min} is not a strict limitation, because in practice the retrieved minimum scanning wavenumber is possible to go beyond k_{min}, particularly for the passive-source surface wave surveys, which might be relevant to the specific data processing algorithms (Park and Carnevale, 2010; Foti et al., 2018; Behm et al., 2019).

Besides, we also notice that the dispersion spectra with shorter array length shows lower imaging resolution compared to that with longer one. Here we employ the array response function (ARF) concept to explain the influence of the array geometry on dispersion measurement (Capon, 1969; Rost and Thomas, 2002; Picozzi et al., 2010; Liu et al., 2020). The array response function is also called the array smoothing function (ASF) or the spectral estimator in some literatures (Johnson and Dudgeon, 1993; Boiero and Socco, 2011; Bergamo et al., 2012), and is usually defined as

$$ARF(k) = |\sum_{j=1}^{N} e^{i2\pi(k-k_0)x_j}|. \quad (7)$$

The green lines on Figure 6b and d indicate the normalized ARFs at 17 Hz. As opposed to a delta function Dirac (1981), the ARF always contains side lobes. The main lobe of the ARF determines the imaging resolution for the slantstacking based dispersion imaging methods (Boiero and Socco, 2011; Cheng et al., 2020). Whereas, the side lobes of the ARF will present as weak wiggles around the dominant dispersion energy, which might be misidentified as weak higher modes or other coherent signals. Moreover, these wiggles (or side lobes) could emphasize interferences from the incoherent noise and smear the dispersion spectra. Cheng et al. (2020) indicates that the phase-weighted slantstacking algorithm is able to attenuate these side lobes effects of ARF on surface wave dispersion images.

3.2 The source-related artifacts

The noise source distributions, in both the time-space domain and the time-frequency domain, have significant influences on passive surface wave dispersion measurements. The complex noise source characteristics make the passive surface wave surveys more challenging compared to the active-source surface wave surveys, especially for the high-frequency ambient noise data in the urban area. It is well known the observed seismic frequency band is finite, and usually depends on the source spectrum distribution. For example, the dominant frequency bands for the traffic-induced passive surface waves are usually from 2 Hz to 20 Hz in an urban area. If we force the mathematical algorithms to measure surface wave dispersion spectra beyond the recorded frequency band, artifacts will be introduced. Moreover, most mathematical algorithms of frequently-used passive surface wave methods only hold under specific noise source distribution assumptions. If the assumption break, for example under the directional noise source distribution, artifacts will be introduced into the linear-array based dispersion measurements. We admit that situations could be complex, so, to keep the consistency of this study we only report two types of most frequently-observed source-related artifacts: artifacts from incoherent noises and artifacts from directional noises.

3.2.1 Artifacts from incoherent noises

According to Bergamo et al. (2012), the computed surface wave dispersion spectra $E(f, k)$ can be taken as a combination of the theoretical dispersion spectrum and the array response function (ARF), which presents as a series of frequency-independent horizontal lines in the $f - k$ domain. When the energy of the measured surface wave is negligible, the computed dispersion spectra will be dominated by contributions from ARF. Here, we present one active-source numerical example to illustrate the dispersion characteristics under this case.

An active-source surface wave shot gather from a two-layer earth model (Table.2) was generated using a finite-difference solver, SOFI2D (Bohlen, 2002), with a 25 Hz ricker wavelet and 30 m nearest offset. The synthetic Rayleigh wave was observed with a 60-channel linear array and 1-m spatial interval (Fig.7a), and the corresponding averaged spectrum shows dominated energy between 5 Hz and 65 Hz as indicated by the blue dash lines. The obtained dispersion spectra in the $f-k$ domain presents great correlation between the spectrum energy (Fig.7b) and the dispersion energy (Fig.7c); a series of horizontal artifacts (indicated by the black arrow), which are co-located with the nearly zero spectrum at two ends in frequency axis, indicate contributions from ARF. In fact, these artifacts are frequently observed on the $f-v$ domain dispersion image but with a different form as a series of radial pattern energy, especially for the passive-source dispersion spectra after the frequency normalization (Fig.7d). Therefore, we call this type of artifacts as radial pattern artifacts. Note that, the type D spatial aliasing is also one special case of radial pattern artifacts. Considering that these artifacts are very common and could seriously pollute the measured dispersion images, we present two field examples to carefully discuss performances of different data processing procedures on attenuation of this type of artifacts .

Field example #1

We provide a passive-source field example to explain the characteristics and the attenuation of the radial pattern artifacts. 5-min ambient noise data were recorded by a linear array of 38 Zland nodes (5 Hz) with 2 ms sampling rate and 1 m spatial-interval. The dataset was first reported by Liu et al. (2020). Although whitening procedure is not included in this noise data preprocessing workflow, clean surface waves are visible on the bin-stacked virtual source gather (Fig.8a). The obtained dispersion spectra using MAPS (Fig.8c) presents two distinct radial pattern artifacts as highlighted by the black dashed line.

In order to figure out the influence of whitening on radial pattern artifacts attenuation, we reprocess the noise data by including the whitening preprocessing procedure prior to cross-correlation. The spectrum of the updated coherent signals (Fig.9b) has been significantly extended at lower frequency band ($<$ 5 Hz), and balanced at higher frequency band ($>$ 15 Hz). We also observe that the radial pattern artifacts have been significantly eliminated with more higher frequency components emerging in both $x-t$ domain (Fig.9a) and the $f-v$ domain (Fig.9c). It indicates spectral whitening makes contributions to attenuation of the radial pattern artifacts for passive-source surface wave dispersion imaging.

According to Prieto et al. (2009), performing cross-correlation C_{x_1,x_2} with spectral whitening is equivalent to calculating the cross-coherence H_{x_1,x_2},

$$H_{x_1,x_2} = \frac{u(x_1,\omega)u^*(x_2,\omega)}{|u(x_1,\omega)||u(x_2,\omega)|}. \quad (8)$$

In terms of attenuation of the radial pattern artifacts, our work implies the cross-coherence algorithm is superior to the cross-correlation in passive-source surface wave imaging (Nakata et al., 2011). Cautions should also be paid because pseudo arrivals generated by spectral whitening or cross-coherence with scattered waves can occur, particularly for at low frequencies (Nakata, 2020). Besides, it is interesting that some spikes on the spectrum (e.g., 22 Hz, 31 Hz, 39 Hz on the pink curves of Fig.9b) seem to be enhanced after whitening, which are also co-located with the spikes (or gaps) on the dispersion spectra (Fig.9c). Unfortunately, we find it is challenging to fully remove these spikes on dispersion spectra, since they are likely associated with some persistent noise sources around the site. Similar phenomenon has been reported in the literatures (e.g., Zeng and Ni, 2010; Gaudot et al., 2016; Cheng et al., 2021b).

Field example #2

According to eq.4, MAPS includes the whole C_N^2 inter-station cross-correlation pairs for dispersion imaging. However, many interferometric passive-source surface wave applications only utilize one virtual-source gather including totally C_N^1 inter-station cross-correlation pairs (e.g., Zhang et al., 2020; Li et al., 2020), because the interpreters usually follow the conventional active-source surface wave (e.g., MASW) acquisition strategy by using single shot gather for dispersion analysis. In this case, lots of useful information might be wasted. Figure 10 shows a comparison of measured ARFs between one virtual-source gather (C_N^1 inter-station pairs) and multiple virtual-sources gather (C_N^2 inter-station pairs). With more inter-station pairs included, the latter one (the black curve on Fig.10) shows smoother side lobes which might decrease the possibility of the interference between the array response artifacts and the incoherent noise (Wu et al., 2017).

We present an example to show performances of the interferometric method (i.e. MAPS) with different virtual-source gathers on attenuation of the radial pattern artifacts. The dataset was first reported by Cheng et al. (2019), which was collected along a busy railway over 30-min using a 24-channel linear array. The spatial interval is 10 m. Ambient noise interferometry is applied to retrieve empirical Green's functions. MAPS is then performed with only one virtual-source gather (C_N^1 inter-station cross-correlation pairs, highlighted on Fig.11a) and with the whole multiple virtual-sources gather (C_N^2 inter-station cross-correlation pairs, Fig.11b), respectively. Compared with the dispersion measurement from one virtual-source gather (Fig.12a), the dispersion measurement from multiple virtual-sources gather (Fig.12b) is more continuous and much cleaner with less distortions and radial pattern artifacts. With more information included as well as spatial averaging, the multiple virtual-sources (C_N^2) gather presents its advantage in coherent signal emergence which contributes to attenuate the radial pattern artifacts.

Nevertheless, we observe that artifacts are not completely attenuated on Figure 12b. To some extent, the leaky artifacts still distort the dispersion energy trend, especially for the high overtones. It is worth noting that spectral whitening has been included during data preprocessing for both Figure 12a and Figure 12b. It implies spectral whitening is not universally applicable for radial pattern artifacts attenuation, either. Data selection is an effective tool for data quality control, and might be an alternative. Studies have successfully applied various data selection strategies on passive-source surface wave imaging for dispersion spectra enhancement (e.g., Cheng et al., 2018b; Zhou et al., 2018; Cheng et al., 2019; Pang et al., 2019; Xi et al., 2020; Liu et al., 2021). We follow Cheng et al. (2019) to present a successful application of radial pattern artifacts attenuation by data selection of train noise in $\tau - p$ domain. We formulate a criterion to detect high signal-to-noise ratio (SNR) data segments under a desired surface velocity range from 200 m/s to 400 m/s, and found an interesting phenomenon (Fig.13a) that time windows, when trains are arriving or departing the observation array, usually show higher SNR than time windows when trains are closely passing the array or far away from the array. It indicates that the data selection strategy provides a chance to carefully analyze noise source characteristics. Next we selectively stack the high quality data segments for dispersion measurement. The dispersion spectra after selective stacking (Fig.13b) has been much improved with the radial pattern artifacts significantly attenuated. The reader is referred to Cheng et al. (2019) for more details about this data selection technique.

3.2.2 Artifacts from directional noises

It is well known that the empirical Green's function can be extracted by cross-correlating two receivers under the randomly distributed noise sources. In practice, the noise source distribution is rarely random. Cheng et al. (2016) indicated that the directional noise sources could produce biased cross-correlations, as well as biased dispersion measurements, particularly for linear receiver arrays. In order to attenuate the azimuthal effect on dispersion measurements, Cheng et al. (2016) proposed to apply azimuthal adjustment to the slant-stacking algorithm. However, it remains a real challenge for azimuth detection using linear array. To address the problem associated with the linear array, Liu et al. (2020) adapted a linear receiver array into a pseudo-linear array by adding two more off-line receivers to increase the array response to off-line signals.

Here, we apply the 2D ARF concept to explain the advantage of the pseudo-linear array on azimuthal effect attention. For consistency, we simply adapt the ARF on eq.7 from 1D to 2D as,

$$ARF(k,\theta) = |\sum_{j=1}^{N} e^{i2\pi k(x_j cos\theta + y_j sin\theta) - ik_0(x_j cos\theta_0 + y_j sin\theta_0)}|, \quad (9)$$

where, x_i and y_i indicate the receiver location in Cartesian coordinates. Since 2D ARF can illustrate the array response or beamforming resolution to a plane wave, we take a plane wave at frequency 15 Hz and velocity 0.3 km/s as example. Figure 14 presents a comparison of ARFs between the linear array (the left panel) and the pseudo-linear array (the right panel). The ARF of the linear array provides multiple beamer peaks which can not focus on the target azimuth and velocity (the pink circle); while the ARF of the adapted pseudo-linear array shows a high resolution response to the input plane wave. It implies the linear array can not solve the 2D beamforming problems that need simultaneously seek azimuth and velocity solutions. Thus, Cheng et al. (2016) suggested defining an average velocity for azimuth detection, while Liu et al. (2020) provided a solution cleverly by using the pseudo-linear array geometry.

4 Discussion

As the first review work on the artifacts in passive surface wave dispersion imaging, we admit that we might not be able to include all the existing artifacts but the summarized artifacts in this work are definitely significant to understand the complexity of surface wave dispersion imaging and will lay a foundation for the further work.

All previously mentioned artifacts, including spatial aliasing, array response artifacts, and radial pattern artifacts, present as individual energy overlying around the true dispersion energy and smearing the energy peaks. Nevertheless, there also exist some artifacts that directly affect the true dispersion energy and produce biased dispersion information, for example, artifacts from the directional noise sources which is summarized as source-related artifacts.

Here, we discuss another type of similar artifacts: artifacts from non-interferometric passive-source methods. Cheng et al. (2020) presents a comprehensive comparison between the non-interferometric methods and the interferometric methods. Numerical tests and field examples demonstrate that non-interferometric methods are less accurate than the interferometric methods when sources are out of line. Compared with the accurate dispersion spectra obtained from the interferometric methods, these biased dispersion energy measured by non-interferometric methods can be taken as artifacts. It is a kind of systematic bias of non-interferometric methods considering the required in-line noise source distribution is rarely achievable.

We present a field example of the artifacts from the non-interferometric methods. The dataset was first reported by Cheng et al. (2020). A linear array of 48 RefTek 125A digitizers was deployed parallel to a busy road with an off-line distance

20∼30m. All digitizers were connected to 2.5 Hz vertical-component geophones. Figure 15 presents a comparison of the obtained dispersion spectra between the non-interferometric methods (PMASW and ReMi) and the interferometric methods (SPAC and MAPS). The little off between the picked dispersion curves from MAPS (the black crosses) and the energy peaks of the non-interferometric methods indicates the biases produced by the non-interferometric methods. To address biases, Louie (2001) indicated that an interpreter must pick the lower edge of energy peaks of phase velocities on the ReMi measurements, rather than the dispersion energy peaks, and hypothesized that the off-line triggered sources caused the higher apparent velocities. However, this bias phenomenon is not unique to the ReMi method but is common to all linear-array-based non-interferometric passive-source surface wave methods. Cheng et al. (2020) provided an alternative to estimate the biases in non-interferometric measurements by using half of the ASF (or ARF) peak (k_h) to quantify the imaging resolution, and assumed the measured biases of non-interferometric methods should be within the imaging resolution range. Therefore, k_h could be taken as a bias indicator during the interpretation of non-interferometric passive surface wave methods.

5 Conclusions

We summarize two groups of artifacts that are frequently observed on passive surface wave dispersion measurements but poorly understand in the past; they include the geometry-related artifacts because of the sparse spatial sampling or the insufficient array coverage, and the source-related artifacts, for example, artifacts from incoherent noises and artifacts from directional noises. Numerical and field examples present how these artifacts are generated and how they can be attenuated. This work might help the reader understand the complexity of the measured dispersion spectra and lead to further improvement on surface wave dispersion analysis. It also suggests:

(1) the shorter spatial interval dx will extend the maximum wavenumber k_{max}, and result in higher maximum frequency limitation that can be observed on dispersion spectra;

(2) the longer array length L will increase the dispersion imaging resolution with the smaller minimum wavenumber k_{min}, and result into lower minimum frequency limitation that can be observed on dispersion spectra;

(3) the spectral whitening is critical to broadening frequency bandwidth for surface wave dispersion imaging, particularly for the passive-source surface wave imaging;

(4) the cross-coherence algorithm is recommended for the applications of the interferometric surface wave methods, since it has the advantage of including spectral

whitening when cross-correlating;

(5) the multiple virtual-sources gather (C_N^2) is prior to the one virtual-source gather (C_N^1) for the interferometric surface wave imaging, which will increase the data utilization and enhance the coherent dispersion energy;

(6) the data selection strategy is effective to attenuate the source-related artifacts, and provides a chance to analyze noise source characteristics.

In general, the limitation of the expense budget usually leads to a dilemma between spatial sampling and spatial coverage. We have to make a trade-off between the higher spatial resolution with the denser array and the deeper depth exploration with the longer array. Nevertheless, a rapidly advancing technique, distributed acoustic sensing (DAS), might provide promising routes to solve these problems, considering DAS in particular allows for acquisition over tens of kilometers while providing spatial sampling in the meter range, thus enabling local surface wave analysis with high fidelity.

Acknowledgements

This study was supported by the Startup Funds of Zhejiang University and the National Natural Science Foundation of China under grant no. 41830103. We thank the SISL team, as well as AoCheng Tech crews, for the field-data acquisitions. We would like to thank Changjiang Zhou, Jingyin Pang, Tianyu Dai and Ya Liu for many useful discussions.

Conflict of interest

The authors declare that they have no conflict of interest.

References

Ajo-Franklin JB, Dou S, Lindsey NJ, Monga I, Tracy C, Robertson M, Rodriguez Tribaldos V, Ulrich C, Freifeld B, Daley T, Li X (2019) Distributed Acoustic Sensing Using Dark Fiber for Near-Surface Characterization and Broadband Seismic Event Detection. Scientific Reports 9(1):1328, DOI 10.1038/s41598-018-36675-8

Aki K (1957) Space and time spectra of stationary stochastic waves, with special reference to microtremors. Bulletin of the Earthquake Research Institute 35:415–456

Aki K (1965) A note on the use of microseisms in determining the shallow structures of the Earth's crust. GEOPHYSICS 30(4):665–666, DOI 10.1190/1.1439640

Ali MY, Barkat B, Berteussen KA, Small J (2013) A low-frequency passive seismic array experiment over an onshore oil field in Abu Dhabi , United Arab Emirates. Geophysics 78(4):B159–B176

Asten M, Hayashi K (2018) Application of the spatial auto-correlation method for shear-wave velocity studies using ambient noise. Surveys in Geophysics 39(4):633–659

Asten MW (2006) On bias and noise in passive seismic data from finite circular array data processed using SPAC methods. Geophysics 7(6):153–162

Asten MW, Yong A, Foti S, Hayashi K, Martin AJ, Stephenson WJ, Cassidy JF, Coleman J, Nigbor R, Castellaro S, et al. (2022) An assessment of uncertainties in VS profiles obtained from microtremor observations in the phased 2018 COSMOS blind trials. Journal of Seismology pp 1–24

Bajaj K, Anbazhagan P (2019) Comprehensive amplification estimation of the Indo Gangetic Basin deep soil sites in the seismically active area. Soil Dynamics and Earthquake Engineering 127:105855

Bakulin A, Calvert R (2006) The virtual source method: Theory and case study. Geophysics 71(4):139–150

Becker G, Knapmeyer-Endrun B (2018) Crustal thickness across the Trans-European Suture Zone from ambient noise autocorrelations. Geophysical Journal International 212(2):1237–1254

Behm M, Leahy GM, Snieder R (2014) Retrieval of local surface wave velocities from traffic noise - an example from the La Barge basin (Wyoming). Geophysical Prospecting 62(2):223–243

Behm M, Nakata N, Bokelmann G (2016) Regional ambient noise tomography in the Eastern Alps of Europe. Pure and Applied Geophysics 173(8):2813–2840

Behm M, Cheng F, Patterson A, Soreghan GS (2019) Passive processing of active nodal seismic data: estimation of vp/vs ratios to characterize structure and hydrology of an alpine valley infill. Solid Earth 10(4):1337–1354, DOI 10.5194/se-10-1337-2019

Bensen GD, Ritzwoller MH, Barmin MP, Levshin AL, Lin F, Moschetti MP, Shapiro NM, Yang Y (2007) Processing seismic ambient noise data to obtain reliable broadband surface wave dispersion measurements. Geophysical Journal International 169:1239–1260

Bergamo P, Boiero D, Socco LV (2012) Retrieving 2D structures from surface-wave data by means of space-varying spatial windowing. GEOPHYSICS 77(4):EN39–EN51, DOI 10.1190/geo2012-0031.1

Bohlen T (2002) Parallel 3-d viscoelastic finite difference seismic modelling. Computers & Geosciences 28(8):887–899

Bohlen T, Kugler S, Klein G, Theilen F (2004) 1.5D inversion of lateral variation of Scholte-wave dispersion. Geophysics 69(2):330, DOI 10.1190/1.1707052

Boiero D, Socco LV (2011) The meaning of surface wave dispersion curves in weakly laterally varying structures. Near Surface Geophysics 9:561–570, DOI 10.3997/1873-0604.2011042

Campillo M, Paul A (2003) Long-range correlations in the diffuse seismic coda. Science 299(5606):547–549

Capon J (1969) High-resolution frequency-wavenumber spectrum analysis. Proceedings of the IEEE 57(8):1408–1418

Cárdenas-Soto M, Piña-Flores J, Escobedo-Zenil D, Vidal-Garcia MC, Natarajan T, Hussain Y, Sánchez-Sesma FJ (2021) Seismic ambient noise tomography to retrieve near-surface properties in soils with significant 3D lateral heterogeneity: the case of Quinta Colorada building in Chapultepec, Mexico. Natural Hazards 108(1):129–145

Castellanos JC, Clayton RW, Juarez A (2020) Using a time-based subarray method to extract and invert noise-derived body waves at Long Beach, California. Journal of Geophysical Research: Solid Earth 125(5), DOI 10.1029/2019JB018855

Chávez-García FJ, Rodríguez M, Stephenson WR (2006) Subsoil structure using SPAC measurements along a line. Bulletin of the Seismological Society of America 96(2):729–736, DOI 10.1785/0120050141

Chen X, Xia J, Pang J, Zhou C, Mi B (2022) Deep learning inversion of Rayleigh-wave dispersion curves with geological constraints for near-surface investigations. Geophysical Journal International 231(1):1–14

Chen Y, Ai Y, Jiang M, Yang Y, Lei J (2021) New insights into potassic intraplate volcanism in Northeast China from joint tomography of ambient noise and teleseismic surface waves. Journal of Geophysical Research: Solid Earth 126(8):e2021JB021856

Cheng F, Xia J, Xu Y, Xu Z, Pan Y (2015) A new passive seismic method based on seismic interferometry and multichannel analysis of surface waves. Journal of Applied Geophysics 117:126–135

Cheng F, Xia J, Luo Y, Xu Z, Wang L, Shen C, Liu R, Pan Y, Mi B, Hu Y (2016) Multi-channel analysis of passive surface waves based on cross-correlations. Geophysics 81(5):EN57–EN66

Cheng F, Xia J, Shen C, Hu Y, Xu Z, Mi B (2018a) Imposing active sources during high-frequency passive surface-wave measurement. Engineering 4(5):685–693

Cheng F, Xia J, Xu Z, Hu Y, Mi B (2018b) Frequency – Wavenumber (FK)-Based Data Selection in High - Frequency Passive Surface Wave Survey. Surveys in Geophysics 39:661–682

Cheng F, Xia J, Behm M, Hu Y, Pang J (2019) Automated Data Selection in the Tau–p Domain: Application to Passive Surface Wave Imaging. Surveys in Geophysics pp 1–18, DOI 10.1007/s10712-019-09530-2

Cheng F, Xia J, Xu Z, Ajo-Franklin J (2020) Comparisons between non-interferometric and interferometric passive surface wave imaging methods - Towards linear receiver array. In: SEG Technical Program Expanded Abstracts 2020, Society of Exploration Geophysicists, pp 2110–2114

Cheng F, Chi B, Lindsey NJ, Dawe TC, Ajo-Franklin JB (2021a) Utilizing distributed acoustic sensing and ocean bottom fiber optic cables for submarine structural characterization. Scientific Reports 11(1):5613, DOI 10.1038/s41598-021-84845-y

Cheng F, Xia J, Ajo-Franklin JB, Behm M, Zhou C, Dai T, Xi C, Pang J, Zhou C (2021b) High-resolution ambient noise imaging of geothermal reservoir using

3C dense seismic nodal array and ultra-short observation. Journal of Geophysical Research: Solid Earth 2019:1–29, DOI 10.1029/2021jb021827

Cheng F, Xia J, Zhang K, Zhou C, Ajo-Franklin JB (2021c) Phase-weighted slant-stacking for surface wave dispersion measurement. Geophysical Journal International pp 256–269, DOI 10.1093/gji/ggab101

Cheng F, Lindsey NJ, Sobolevskaia V, Dou S, Freifeld B, Wood T, James SR, Wagner AM, Ajo-Franklin JB (2022) Watching the cryosphere thaw: Seismic monitoring of permafrost degradation using distributed acoustic sensing during a controlled heating experiment. Geophysical Research Letters 49(10):e2021GL097195

Cho I, Iwata T (2021) Limits and benefits of the spatial autocorrelation microtremor array method due to the incoherent noise, with special reference to the analysis of long wavelength ranges. Journal of Geophysical Research: Solid Earth 126(2):e2020JB019850

Cho I, Tada T, Shinozaki Y (2008) Assessing the applicability of the spatial autocorrelation method: A theoretical approach. Journal of Geophysical Research 113(B6):1–19, DOI 10.1029/2007jb005245

Dai T, Hu Y, Ning L, Cheng F, Pang J (2018) Effects due to aliasing on surface-wave extraction and suppression in frequency-velocity domain. Journal of Applied Geophysics 158:71–81, DOI 10.1016/j.jappgeo.2018.07.011

Dai T, Xia J, Ning L, Xi C, Liu Y, Xing H (2021) Deep learning for extracting dispersion curves. Surveys in Geophysics 42(1):69–95

Dirac PAM (1981) The principles of quantum mechanics. 27, Oxford university press

Dorman J, Ewing M (1962) Numerical inversion of seismic surface wave dispersion data and crust-mantle structure in the new york-pennsylvania area. Journal of Geophysical Research 67(13):5227–5241

Dou S, Lindsey N, Wagner AM, Daley TM, Freifeld B, Robertson M, Peterson J, Ulrich C, Martin ER, Ajo-Franklin JB (2017) Distributed Acoustic Sensing for seismic monitoring of the near surface: A traffic-noise interferometry case study. Scientific Reports 7(1):11620, DOI 10.1038/s41598-017-11986-4

Draganov D, Campman X, Thorbecke J, Verdel A, Wapenaar K (2009) Reflection images from ambient seismic noise. Geophysics 74(5):A63–A67

Duncan G, Beresford G (1995) Median filter behaviour with seismic data 1. Geophysical prospecting 43(3):329–345

Ekström G, Abers GA, Webb SC (2009) Determination of surface-wave phase velocities across USArray from noise and Aki's spectral formulation. Geophysical Research Letters 36(18), DOI 10.1029/2009gl039131

Forbriger T (2003) Inversion of shallow-seismic wavefields: I. Wavefield transformation. Geophysical Journal International 153(3):719–734, DOI 10.1046/j.1365-246X.2003.01929.x

Foti S, Parolai S, Albarello D, Picozzi M (2011) Application of surface-wave methods for seismic site characterization. Surveys in geophysics 32(6):777–825

Foti S, Lai CG, Rix GJ, Strobbia C (2014) Surface wave methods for near-surface site characterization. CRC press

Foti S, Hollender F, Garofalo F, Albarello D, Asten M, Bard PY, Comina C, Cornou C, Cox B, Di Giulio G, et al. (2018) Guidelines for the good practice of surface wave analysis: A product of the interpacific project. Bulletin of Earthquake Engineering 16(6):2367–2420

Fu L, Pan L, Li Z, Dong S, Ma Q, Chen X (2022) Improved high-resolution 3d vs model of long beach, ca: Inversion of multimodal dispersion curves from ambient noise of a dense array. Geophysical Research Letters 49(4):e2021GL097619

Gaudot I, Beucler, Mocquet A, Schimmel M, Le Feuvre M, Feuvre ML, Gaudot I (2016) Statistical redundancy of instantaneous phases : theory and application to the seismic ambient wavefield. Geophysical Journal International 204(2):1159–1163, DOI 10.1093/gji/ggv501

Groos JC, Ritter JRR (2009) Time domain classification and quantification of seismic noise in an urban environment. Geophysical Journal International 179(2):1213–1231, DOI 10.1111/j.1365-246X.2009.04343.x

Haney MM, Mikesell TD, van Wijk K, Nakahara H (2012) Extension of the spatial autocorrelation (spac) method to mixed-component correlations of surface waves. Geophysical Journal International 191(1):189–206

Hayashi K, Cakir R, Walsh TJ (2013) Using two-station microtremor array method to estimate shear-wave velocity profiles in Seattle and Olympia, Washington. In: Symposium on the Application of Geophysics to Engineering and Environmental Problems 2013, Society of Exploration Geophysicists and Environment and Engineering, pp 442–451

Hayashi K, Asten MW, Stephenson WJ, Cornou C, Hobiger M, Pilz M, Yamanaka H (2022) Microtremor array method using spatial autocorrelation analysis of Rayleigh-wave data. Journal of Seismology pp 1–27

Hu S, Luo S, Yao H (2020) The frequency-bessel spectrograms of multicomponent cross-correlation functions from seismic ambient noise. Journal of Geophysical Research: Solid Earth 125(8):e2020JB019630

Ivanov J, Park CB, Miller RD, Xia J (2005) Analyzing and Filtering Surface-Wave Energy By Muting Shot Gathers. Journal of Environmental & Engineering Geophysics 10(3):307–322

Johnson D, Dudgeon D (1993) Array signal processing: PTR Prentice Hall. Englewood Cliffs, N J p 533

Kita T, Hayashi K, Bingol H (2011) The development of a 2-dimensional microtremor survey method based on SPAC method using sequential linear arrays. In: 24rd EEGS Symposium on the Application of Geophysics to Engineering and Environmental Problems, European Association of Geoscientists & Engineers, pp cp–247

Lacoss RT, Kelly EJ, Toksöz MN (1969) Estimation of seismic noise structure using arrays. Geophysics 34(1):21–38

Lawrence JF, Denolle M, Seats KJ, Prieto Ga (2013) A numeric evaluation of attenuation from ambient noise correlation functions. Journal of Geophysical Research: Solid Earth 118(12):6134–6145

Lepore S, Grad M (2020) Relation between ocean wave activity and wavefield of the ambient noise recorded in northern poland. Journal of Seismology 24(6):1075–1094

Li YE, Nilot E, Feng X (2020) Observation of guided and reflection P-waves in urban ambient noise cross-correlograms. In: SEG Technical Program Expanded Abstracts 2020, Society of Exploration Geophysicists, pp 2100–2104

Li Z, Lynn W, Chambers R, Larner K, Abma R (1991) Enhancements to prestack frequency-wavenumber (fk) migration. Geophysics 56(1):27–40

Lin FC, Moschetti MP, Ritzwoller MH (2008) Surface wave tomography of the western United States from ambient seismic noise: Rayleigh and Love wave phase velocity maps. Geophysical Journal International 173(1):281–298

Lin FC, Ritzwoller MH, Snieder R (2009) Eikonal tomography: surface wave tomography by phase front tracking across a regional broad-band seismic array. Geophysical Journal International 177(3):1091–1110

Liu Y, Xia J, Cheng F, Xi C, Shen C, Zhou C (2020) Pseudo-linear-array analysis of passive surface waves based on beamforming. Geophysical Journal International pp 640–650, DOI 10.1093/gji/ggaa024

Liu Y, Xia J, Xi C, Dai T, Ning L (2021) Improving the retrieval of high-frequency surface waves from ambient noise through multichannel-coherency-weighted stack. Geophysical Journal International 227(2):776–785

Louie J, Pullammanappallil S, Pancha A, West T, Hellmer W (2011) Earthquake hazard class mapping by parcel in Las Vegas Valley. In: Structures Congress 2011, pp 1794–1805

Louie JN (2001) Faster, Better: Shear-Wave Velocity to 100 Meters Depth from Refraction Microtremor Arrays. Bulletin of the Seismological Society of America 91(2):347–364

Louie JN, Pancha A, Kissane B (2021) Guidelines and pitfalls of refraction microtremor surveys. Journal of Seismology pp 1–16

Luo Y, Xia J, Miller RD, Xu Y, Liu J, Liu Q (2008) Rayleigh-Wave Dispersive Energy Imaging Using a High-Resolution Linear Radon Transform. Pure and Applied Geophysics 165(5):903–922, DOI 10.1007/s00024-008-0338-4

Margaryan S, Yokoi T, Hayashi K (2009) Experiments on the stability of the spatial autocorrelation method (SPAC) and linear array methods and on the imaginary part of the SPAC coefficients as an indicator of data quality. Exploration Geophysics 40(1):121–131

Mi B, Xia J, Tian G, Shi Z, Xing H, Chang X, Xi C, Liu Y, Ning L, Dai T, et al. (2022) Near-surface imaging from traffic-induced surface waves with dense linear arrays: an application in the urban area of hangzhou, china. Geophysics 87(2):B145–B158

Mikesell TD, Gribler G, Xu Z, Haney MM, et al. (2017) High-resolution dispersion images from deblurred masw. In: 2017 SEG International Exposition and Annual Meeting, Society of Exploration Geophysicists

Miller RD, Xia J, Park CB, Ivanov JM (1999) Multichannel analysis of surface waves to map bedrock. The Leading Edge 18(12):1392–1396

Nakahara H (2006) A systematic study of theoretical relations between spatial correlation and Green's function in one-, two- and three-dimensional random scalar wavefields. Geophysical Journal International 167(3):1097–1105, DOI 10.1111/j.1365-246X.2006.03170.x

Nakata N (2020) Pseudo arrivals generated by frequency normalization for seismic interferometry with scattered waves—stationary-phase analysis. In: SEG Technical Program Expanded Abstracts 2020, Society of Exploration Geophysicists, pp 2085–2089

Nakata N, Snieder R, Tsuji T, Larner K, Matsuoka T (2011) Shear wave imaging from traffic noise using seismic interferometry by cross-coherence. Geophysics 76(6):SA97–SA106

Nakata N, Chang JP, Lawrence JF, Boué P (2015) Body wave extraction and tomography at Long Beach, California, with ambient-noise interferometry. Journal of Geophysical Research: Solid Earth 120(2):1159–1173, DOI 10.1002/2015JB011870

Nakata N, Boué P, Brenguier F, Roux P, Ferrazzini V, Campillo M (2016) Body and surface wave reconstruction from seismic noise correlations between arrays at Piton de la Fournaise volcano. Geophysical Research Letters 43, DOI 10.1002/2015GL066997

Ning L, Xia J, Dai T, Liu Y, Zhang H, Xi C (2022) High-Frequency Surface-Wave Imaging from Traffic-Induced Noise by Selecting In-line Sources. Surveys in Geophysics 43(6):1873–1899

O'Connell DRH, Turner JP (2011) Interferometric Multichannel Analysis of Surface Waves (IMASW). Bulletin of the Seismological Society of America 101(5):2122–2141

Okada H, Suto K (2003) The microtremor survey method. Society of Exploration Geophysicists

Paitz P, Sager K, Fichtner A (2019) Rotation and strain ambient noise interferometry. Geophysical Journal International 216(3):1938–1952

Pan Y, Xia J, Xu Y, Xu Z, Cheng F, Xu H, Gao L (2016) Delineating Shallow S -Wave Velocity Structure Using Multiple Ambient-Noise Surface-Wave Methods: An Example from Western Junggar, China. Bulletin of the Seismological Society of America 106(2):327–336, DOI 10.1785/0120150014

Pancha A, Anderson JG, Louie JN, Pullammanappallil SK (2008) Measurement of shallow shear wave velocities at a rock site using the remi technique. Soil Dynamics and Earthquake Engineering 28(7):522–535

Pancha A, Pullammanappallil SK, West LT, Louie JN, Hellmer WK (2017) Large-scale earthquake-Hazard class mapping by parcel in Las Vegas Valley, Nevada. Bulletin of the Seismological Society of America 107(2):741–749

Pang J, Cheng F, Shen C, Dai T, Ning L, Zhang K (2019) Automatic passive data selection in time domain for imaging near-surface surface waves. Journal of Applied Geophysics 162:108–117

Park C, Miller R, Laflen D, Neb C, Ivanov J, Bennett B, Huggins R (2004) Imaging dispersion curves of passive surface waves. In: SEG technical program expanded abstracts 2004, Society of Exploration Geophysicists, pp 1357–1360

Park CB, Carnevale M (2010) Optimum MASW Survey—Revisit after a Decade of Use. In: GeoFlorida 2010: Advances in Analysis, Modeling & Design, American Society of Civil Engineers, Orlando, Florida, United States, pp 1303–1312, DOI 10.1061/41095(365)130

Park CB, Miller RD, Xia J, Survey KG (1998) Imaging dispersion curves of surface waves on multi-channel record. SEG Expanded Abstracts 17(1):1377–1380

Park CB, Miller RD, Ivanov J (2002) Filtering Surface Waves. In: Symposium on the Application of Geophysics to Engineering and Environmental Problems 2002, Environment and Engineering Geophysical Society, Figure 1, pp SEI9–SEI9, DOI 10.4133/1.2927182

Picozzi M, Parolai S, Bindi D (2010) Deblurring of frequency-wavenumber images from small-scale seismic arrays. Geophysical Journal International 181(1):357–368, DOI 10.1111/j.1365-246X.2009.04471.x

Poupinet G, Ellsworth W, Frechet J (1984) Monitoring velocity variations in the crust using earthquake doublets: An application to the calaveras fault, california. Journal of Geophysical Research: Solid Earth 89(B7):5719–5731

Prieto G, Lawrence J, Beroza G (2009) Anelastic Earth structure from the coherency of the ambient seismic field. Journal of Geophysical Research: Solid Earth 114(B7)

Rafaely B, Weiss B, Bachmat E (2007) Spatial aliasing in spherical microphone arrays. IEEE Transactions on Signal Processing 55(3):1003–1010

Rost S, Thomas C (2002) Array seismology: Methods and applications. Reviews of Geophysics 40(3):1008, DOI 10.1029/2000RG000100

Roy N, Jakka RS (2017) Near-field effects on site characterization using MASW technique. Soil Dynamics and Earthquake Engineering 97:289–303, DOI 10.1016/j.soildyn.2017.02.011

Schwab F, Knopoff L (1972) Fast surface wave and free mode computations. In: Methods in Computational Physics: Advances in Research and Applications, vol 11, Elsevier, pp 87–180

Shapiro NM, Campillo M (2004) Emergence of broadband Rayleigh waves from correlations of the ambient seismic noise. Geophysical Research Letters 31(7)

Shirzad T, Shomali ZH, Naghavi M, Norouzi R (2015) Near-surface vs structure by inversion of surface wave estimated from ambient seismic noise. Near Surface Geophysics 13(5):447–455

Snieder R (2004) Extracting the green's function from the correlation of coda waves: A derivation based on stationary phase. Physical Review E 69(4):046610

Snieder R, Miyazawa M, Slob E, Vasconcelos I, Wapenaar K (2009) A Comparison of Strategies for Seismic Interferometry. Surveys in Geophysics 30(4-5):503–523, DOI 10.1007/s10712-009-9069-z

Socco LV, Foti S, Boiero D (2010) Surface-wave analysis for building near-surface velocity models—established approaches and new perspectives. Geophysics 75(5):75A83–75A102

Stein EM, Shakarchi R (2011) Fourier analysis: an introduction, vol 1. Princeton University Press

Stephenson WJ, Louie JN, Pullammanappallil S, Williams R, Odum JK (2005) Blind shear-wave velocity comparison of remi and masw results with boreholes to 200 m in santa clara valley: implications for earthquake ground-motion assessment. Bulletin of the Seismological Society of America 95(6):2506–2516

Strobbia C, Cassiani G (2011) Refraction microtremors: Data analysis and diagnostics of key hypotheses. Geophysics 76(3), DOI 10.1190/1.3560246

Thorson JR, Claerbout JF (1985) Velocity-stack and slant-stack stochastic inversion. Geophysics 50(12):2727–2741

Tibuleac IM, von Seggern D (2012) Crust-mantle boundary reflectors in nevada from ambient seismic noise autocorrelations. Geophysical Journal International 189(1):493–500

Tromp J, Luo Y, Hanasoge S, Peter D (2010) Noise cross-correlation sensitivity kernels. Geophysical Journal International 183(2):791–819

Tsai VC, Moschetti MP (2010) An explicit relationship between time-domain noise correlation and spatial autocorrelation (SPAC) results. Geophysical Journal International 182(1):454–460, DOI 10.1111/j.1365-246X.2010.04633.x

Tsai VC, Sager K (2022) The relationship between cross correlations and green's functions in ambient noise interferometry with bayesian constraints. Geophysical Journal International 228(2):816–825

Turner G (1990) Aliasing in the tau-p transform and the removal of spatially aliased coherent noise. Geophysics 55(11):1496–1503

Vantassel JP, Cox BR (2022) SWprocess: a workflow for developing robust estimates of surface wave dispersion uncertainty. Journal of Seismology pp 1–26

Wang J, Wu G, Chen X (2019) Frequency-Bessel transform method for effective imaging of higher-mode Rayleigh dispersion curves from ambient seismic noise data. Journal of Geophysical Research: Solid Earth 124(4):3708–3723

Wapenaar K (2004) Retrieving the elastodynamic green's function of an arbitrary inhomogeneous medium by cross correlation. Physical Review Letters 93(25):254301

Wapenaar K, van der Neut J, Ruigrok E, van der Neut J (2008) Passive seismic interferometry by multidimensional deconvolution. Geophysics 73(NO.6):A51—-A56

Wu D, Sun C, Lin M (2017) Activeseismic surface wave dispersion imaging method based on cross-correlation and phase-shifting (in Chinese). Progress in Geophysics 32(4):533, DOI 10.6038/pg20170437

Wu Gx, Pan L, Wang Jn, Chen X (2020) Shear velocity inversion using multimodal dispersion curves from ambient seismic noise data of usarray transportable array. Journal of Geophysical Research: Solid Earth 125(1):e2019JB018213

Xi C, Mi B, Dai T, Liu Y, Ning L (2020) Spurious signals attenuation using SVD-based Wiener filter for near-surface ambient noise surface wave imaging. Journal of Applied Geophysics 183:104220

Xi C, Xia J, Mi B, Dai T, Liu Y, Ning L (2021) Modified frequency–Bessel transform method for dispersion imaging of Rayleigh waves from ambient seismic noise. Geophysical Journal International 225(2):1271–1280

Xia J, Miller RD, Park CB (1999) Estimation of near-surface shear-wave velocity by inversion of Rayleigh waves. Geophysics 64(3):691–700

Xia J, Miller RD, Park CB, Ivanov J (2000) Construction of 2-d vertical shear-wave velocity field by the multichannel analysis of surface wave technique. In: 13th EEGS Symposium on the Application of Geophysics to Engineering and Environmental Problems, European Association of Geoscientists & Engineers, pp cp–200

Xia J, Miller RD, Xu Y, Luo Y, Chen C, Liu J, Ivanov J, Zeng C (2009) High-frequency Rayleigh-wave method. Journal of Earth Science 20(3):563–579

Xu X, Li G, Ding Z, Huang X (2022) S-Wave velocity structure of the crust and upper mantle beneath the north China craton determined by joint inversion of Rayleigh-wave phase velocity and Z/H Ratio. Seismological Research Letters

Xu Y, Zhang B, Luo Y, Xia J (2013) Surface-wave observations after integrating active and passive source data. The Leading Edge 32(6):634–637

Xu Z, Xia J, Luo Y, Cheng F, Pan Y (2016) Potential misidentification of love-wave phase velocity based on three-component ambient seismic noise. Pure and Applied Geophysics 173(4):1115–1124

Xu Z, Dylan Mikesell T, Xia J, Cheng F (2017) A comprehensive comparison between the refraction microtremor and seismic interferometry methods for phase-velocity estimation. Geophysics 82(6):EN99–EN108

Yan FG, Cao B, Rong JJ, Shen Y, Jin M (2016) Spatial aliasing for efficient direction-of-arrival estimation based on steering vector reconstruction. EURASIP Journal on Advances in Signal Processing 2016(1):1–8

Yang Y, Ritzwoller MH, Levshin AL, Shapiro NM (2007) Ambient noise Rayleigh wave tomography across Europe. Geophysical Journal International 168(1):259–274

Yao H, van der Hilst RD (2009) Analysis of ambient noise energy distribution and phase velocity bias in ambient noise tomography, with application to SE Tibet. Geophysical Journal International 179(2):1113–1132

Zeng X, Ni S (2010) A persistent localized microseismic source near the Kyushu Island, Japan. Geophysical Research Letters 37(24):8–13, DOI 10.1029/2010GL045774

Zhan Z (2020) Distributed acoustic sensing turns fiber-optic cables into sensitive seismic antennas. Seismological Research Letters 91(1):1–15

Zhang K, Li H, Wang X, Wang K (2020) Retrieval of shallow S-wave profiles from seismic reflection surveying and traffic-induced noise. Geophysics 85(6):EN105–EN117

Zhou C, Xi C, Pang J, Liu Y (2018) Ambient noise data selection based on the asymmetry of cross-correlation functions for near surface applications. Journal of Applied Geophysics 159:803–813

Zhou HW (2014) Practical seismic data analysis. Cambridge University Press

Zywicki DJ, Rix GJ (2005) Mitigation of Near-Field Effects for Seismic Surface Wave Velocity Estimation with Cylindrical Beamformers. Journal of Geotechnical and Geoenvironmental Engineering 131(8):970–977, DOI 10.1061/(ASCE)1090-0241(2005)131:8(970)

Layer number	$\mathbf{V_p}(m/s)$	$\mathbf{V_s}(m/s)$	$\boldsymbol{\rho}(g/cm^3)$	$\mathbf{h}(m)$
1	400	800	2.0	10
2	200	400	2.0	10
3	600	1200	2.0	10
Half-space	800	1600	2.0	Infinite

Table 1: Parameters of a four-layer model.

Layer number	$\mathbf{V_p}(m/s)$	$\mathbf{V_s}(m/s)$	$\boldsymbol{\rho}(g/cm^3)$	$\mathbf{h}(m)$
1	200	800	2.0	10
Half-space	400	1200	2.0	Infinite

Table 2: Parameters of a two-layer model.

List of Tables

1 Parameters of a four-layer model. 33
2 Parameters of a two-layer model. 33

List of Figures

1 Flowchart for the passive-source surface wave methods, including non-interferometric and interferometric techniques. 37

2 Comparison of the characteristics of the predicted spatial aliasing between different spatial sampling, $dx = 2m$ (a) and $dx = 10m$ (b). The black dashed curves show the theoretical dispersion curves calculated from a four-layer earth model (Tab.1) by Knopoff's method (Schwab and Knopoff, 1972); four colored curves represent four types of predicted spatial aliasing, A (red diamonds, eq.6a), B (blue triangles, eq.6b), C (black dots, eq.6c), D (green dashed line, eq.6d), respectively. 38

3 A field example of the type A and B spatial aliasing (modified from Dai et al. (2018)). (a). a 145-channel common-shot-point (CSP) gather with 10 m spatial interval and 29.5 m nearest offset; (b). the obtained dispersion measurement by using the phase-shift method. The red dotted line indicates the weak air wave energy; the red diamond curves represent the predicted type A spatial aliasing from air wave; the blue dotted line indicates the non-dispersive body wave energy; the blue dash-dot curves represent the predicted type B spatial aliasing. The good match between the predicted aliasing and the observed artifacts convinces us of the derivation of spatial aliasing (eq.6). Note that, the predicted aliasing artifacts of surface waves are beyond the current spectra window range with velocities lower than 0.1 km/s at a frequency band 1∼9 Hz. 39

4 A field example of the type C spatial aliasing (modified from (Cheng et al., 2018b)). (a1-c1) present the obtained dispersion spectra using different passive-source surface wave imaging methods, PMASW, MAPS, and SPAC, respectively. (a2) and (c2) present the PMASW and SPAC measurements after artifacts attenuated. The black dotted curves represent the predicted type C spatial aliasing based on the picked dispersion curve from MAPS in b1; the blue triangles indicate the predicted type B spatial aliasing. 40

5 A field example of the type D spatial aliasing (modified from Cheng et al. (2015)). (a). the bin-stacked virtual source gather retrieved from ambient noise interferometry; (b) and (c). the obtained dispersion measurements using MAPS before and after aliasing attenuated. The green dashed line indicates the predicted spatial aliasing. 41

6 Effects of array lengths, 100 m (the upper panels) and 20 m (the bottom panels), on MAPS measurements. (a) and (c) show the same source configurations for two different receiver arrays, 100 m and 20 m, respectively; (b) and (d) display the corresponding MAPS measurements in $f-k$ domain. The blue dotted lines indicate the minimum wavenumber (or the maximum wavelength) inferred from the array length; the black dashed lines represent the theoretical dispersion curves; the green curves indicate the normalized ARF curve at 17 Hz. The receiver intervals of both arrays are consistent with $dx=1$. Note that no data preprocessing procedures, except for the segment splitting, are included prior to cross-correlation during MAPS measurements. 42

7 A numerical example of the radial pattern artifacts due to incoherent noises. (a). A synthetic active-source surface wave shot gather; (b) presents the averaged spectrum; (c) and (d) show the obtained dispersion spectra using the phase-shift method in $f-k$ domain and $f-v$ domain. The black dashed line on d represents the theoretical dispersion curve; the blue dash lines on c and d indicate the end frequencies, 5 Hz and 65 Hz, where the spectrum amplitudes are approaching zero. The black dashed arrows on c indicate the artifacts with constant wavenumber; the black dashed arrows on d indicate the corresponding radial pattern artifacts. 43

8 A field example of the radial pattern artifacts (modified from Liu et al. (2020)). (a). The bin-stacked virtual source gather retrieved from ambient noise interferometry without noise data preprocessing. The bin-size is 1 m. (b) The averaged spectrum of a; (c). Dispersion measurement with distinct artifacts. The black dashed lines highlight the radial pattern artifacts. 44

9 Same as Fig.8 but with spectral whitening included prior to cross-correlation. 44

10 A comparison of ARFs between one virtual-source gather (C_N^1, the black solid line) and multiple virtual-sources gather (C_N^2, the red dashed line). Here we take an array of 24 sensors with 10 m spatial interval as an example. 45

11 An example of C_N^2 inter-station cross-correlation for field example #2. (a). Virtual source and virtual receiver configuration for C_N^2 inter-station cross-correlation pairs. (b). The extracted C_N^2 inter-station cross-correlation pairs using ambient noise interferometry. The yellow boxes highlight the source and receiver configuration (a) and cross-correlation pairs (b) for one virtual-source gather with the first trace as the virtual source. 46

12 A field example of radial pattern artifacts and their attenuation (modified from Cheng et al. (2019)). (a). Dispersion spectra of MAPS by using the one virtual-source gather. (b). Dispersion spectra of MAPS by using the multiple virtual-sources gather. The black dashed lines indicate the radial pattern artifacts. 47

13 Attenuation of the radial pattern artifacts in Fig.12 using the data-selection technique (modified from Cheng et al. (2019)). (a) displays the estimated SNR indicators using p energy for each time segment during the 30-min observation. The red dotts indicate the selected time segments with p SNR greater than the defined threshold value, 2. (b) shows the enhanced MAPS measurement with radial pattern artifacts significantly attenuated. The blue dotted line indicates the minimum wavenumber reference, and the blue dashed line indicates the maximum wavenumber reference. 48

14 Array responses for the linear array (a) and the pseudo-linear array (b). The black dots denote the receivers; the black arrows indicate the plane wave; the pink circles indicate the target azimuth and velocity solution. 49

15 A field example of the artifacts from the non-interferometric methods (modified from Cheng et al. (2020)). (a)-(d) present the obtained dispersion spectra using different passive-source surface wave imaging methods, PMASW, ReMi, SPAC, and MAPS, respectively. 50

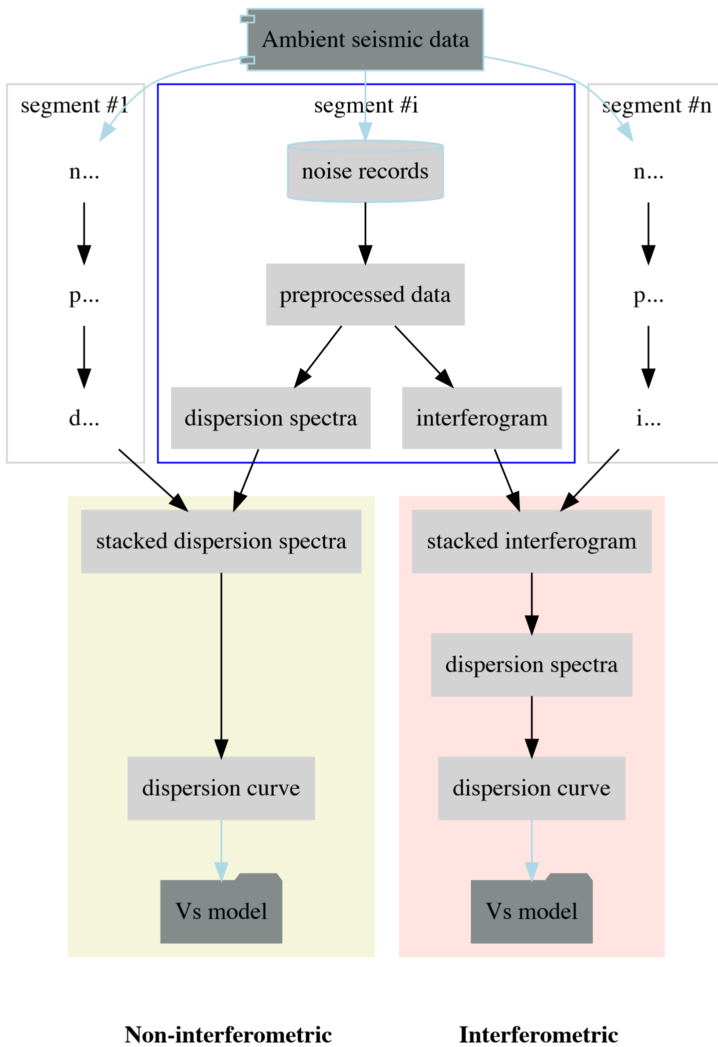

Figure 1: Flowchart for the passive-source surface wave methods, including non-interferometric and interferometric techniques.

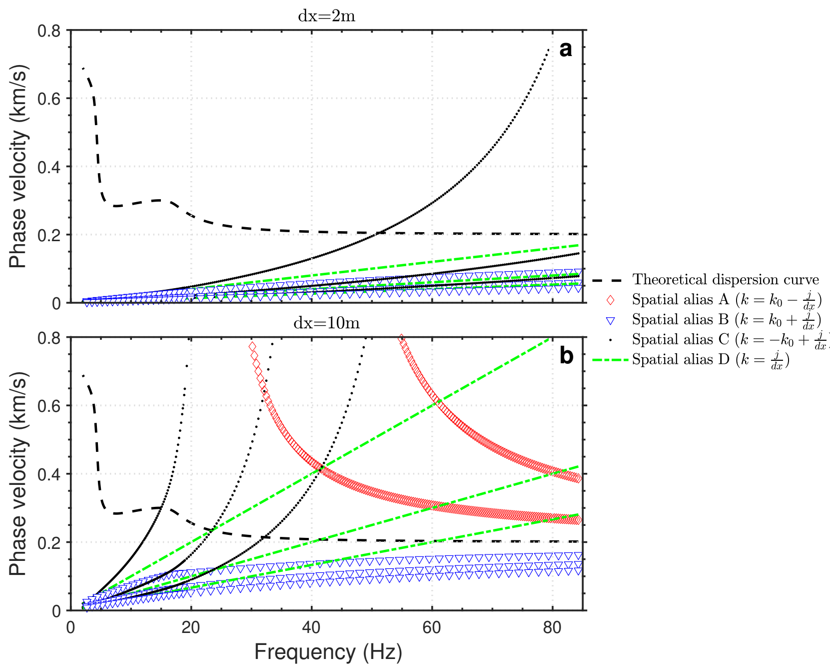

Figure 2: Comparison of the characteristics of the predicted spatial aliasing between different spatial sampling, $dx = 2m$ (a) and $dx = 10m$ (b). The black dashed curves show the theoretical dispersion curves calculated from a four-layer earth model (Tab.1) by Knopoff's method (Schwab and Knopoff, 1972); four colored curves represent four types of predicted spatial aliasing, A (red diamonds, eq.6a), B (blue triangles, eq.6b), C (black dots, eq.6c), D (green dashed line, eq.6d), respectively.

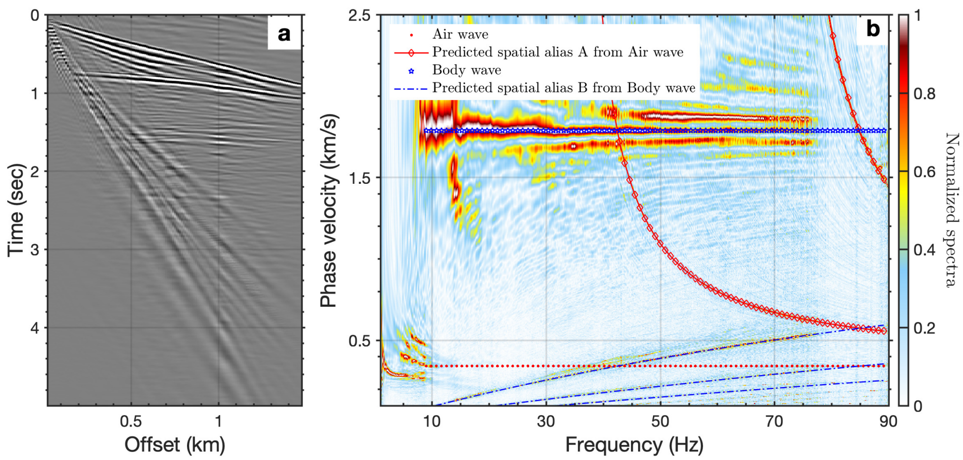

Figure 3: A field example of the type A and B spatial aliasing (modified from Dai et al. (2018)). (a). a 145-channel common-shot-point (CSP) gather with 10 m spatial interval and 29.5 m nearest offset; (b). the obtained dispersion measurement by using the phase-shift method. The red dotted line indicates the weak air wave energy; the red diamond curves represent the predicted type A spatial aliasing from air wave; the blue dotted line indicates the non-dispersive body wave energy; the blue dash-dot curves represent the predicted type B spatial aliasing. The good match between the predicted aliasing and the observed artifacts convinces us of the derivation of spatial aliasing (eq.6). Note that, the predicted aliasing artifacts of surface waves are beyond the current spectra window range with velocities lower than 0.1 km/s at a frequency band 1∼9 Hz.

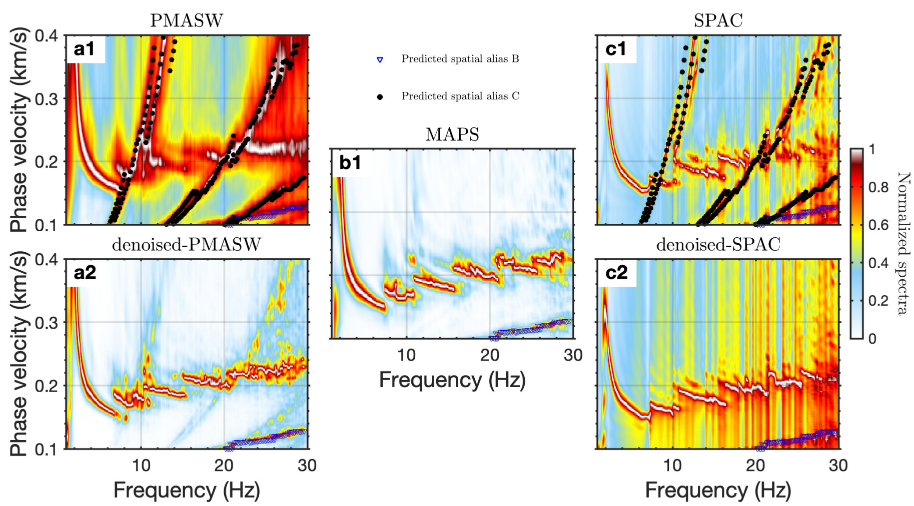

Figure 4: A field example of the type C spatial aliasing (modified from (Cheng et al., 2018b)). (a1-c1) present the obtained dispersion spectra using different passive-source surface wave imaging methods, PMASW, MAPS, and SPAC, respectively. (a2) and (c2) present the PMASW and SPAC measurements after artifacts attenuated. The black dotted curves represent the predicted type C spatial aliasing based on the picked dispersion curve from MAPS in b1; the blue triangles indicate the predicted type B spatial aliasing.

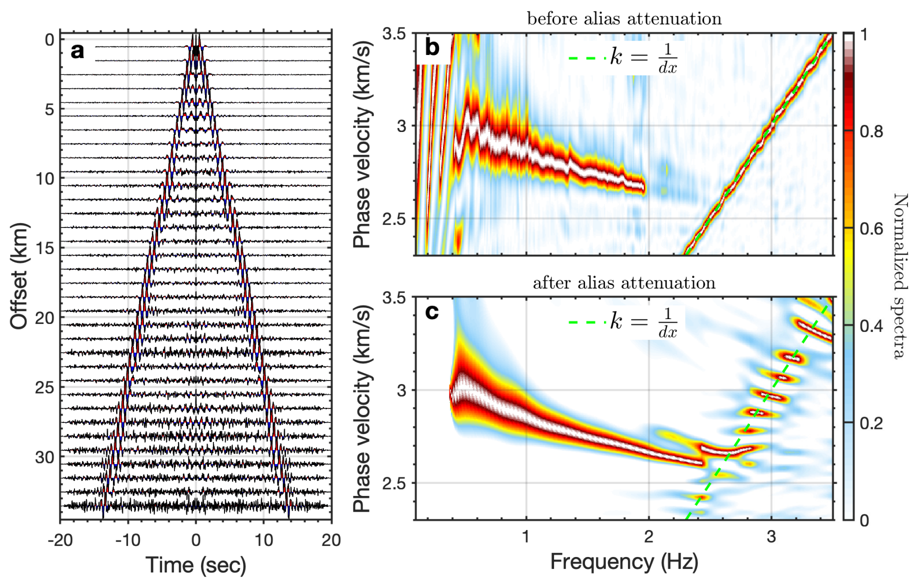

Figure 5: A field example of the type D spatial aliasing (modified from Cheng et al. (2015)). (a). the bin-stacked virtual source gather retrieved from ambient noise interferometry; (b) and (c). the obtained dispersion measurements using MAPS before and after aliasing attenuated. The green dashed line indicates the predicted spatial aliasing.

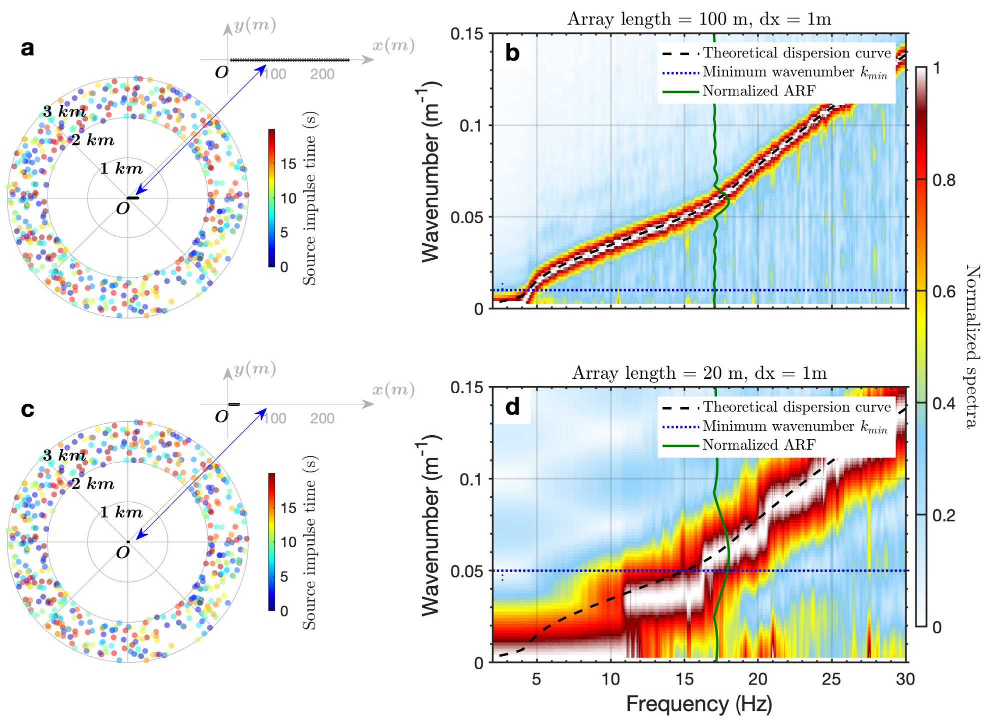

Figure 6: Effects of array lengths, 100 m (the upper panels) and 20 m (the bottom panels), on MAPS measurements. (a) and (c) show the same source configurations for two different receiver arrays, 100 m and 20 m, respectively; (b) and (d) display the corresponding MAPS measurements in $f-k$ domain. The blue dotted lines indicate the minimum wavenumber (or the maximum wavelength) inferred from the array length; the black dashed lines represent the theoretical dispersion curves; the green curves indicate the normalized ARF curve at 17 Hz. The receiver intervals of both arrays are consistent with $dx = 1$. Note that no data preprocessing procedures, except for the segment splitting, are included prior to cross-correlation during MAPS measurements.

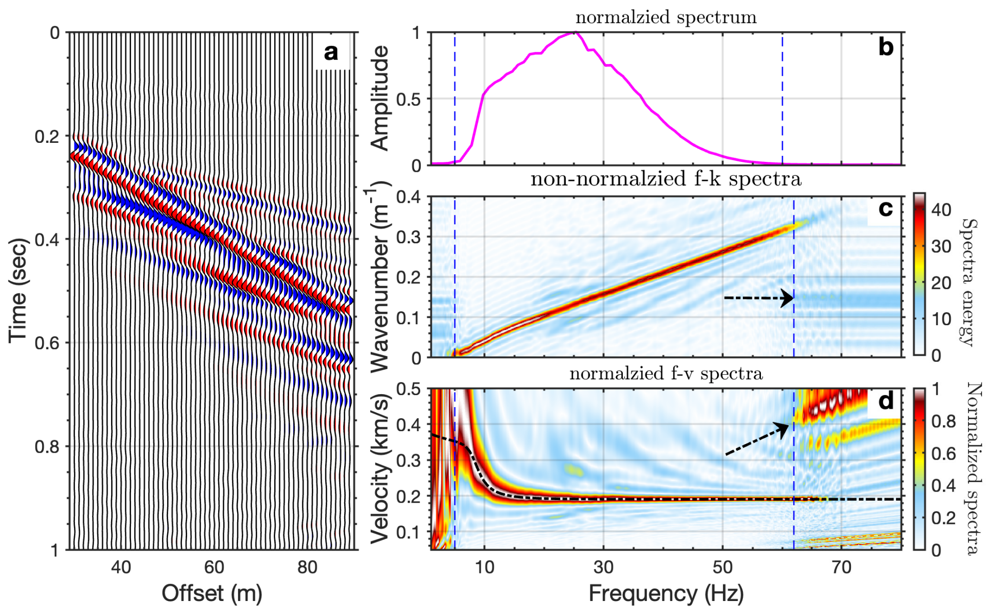

Figure 7: A numerical example of the radial pattern artifacts due to incoherent noises. (a). A synthetic active-source surface wave shot gather; (b) presents the averaged spectrum; (c) and (d) show the obtained dispersion spectra using the phase-shift method in $f-k$ domain and $f-v$ domain. The black dashed line on d represents the theoretical dispersion curve; the blue dash lines on c and d indicate the end frequencies, 5 Hz and 65 Hz, where the spectrum amplitudes are approaching zero. The black dashed arrows on c indicate the artifacts with constant wavenumber; the black dashed arrows on d indicate the corresponding radial pattern artifacts.

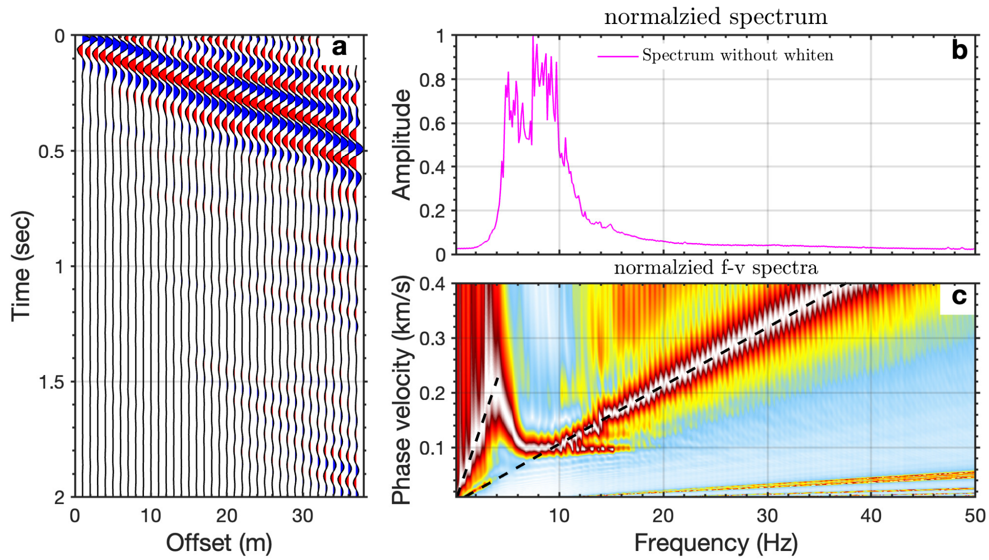

Figure 8: A field example of the radial pattern artifacts (modified from Liu et al. (2020)). (a). The bin-stacked virtual source gather retrieved from ambient noise interferometry without noise data preprocessing. The bin-size is 1 m. (b) The averaged spectrum of a; (c). Dispersion measurement with distinct artifacts. The black dashed lines highlight the radial pattern artifacts.

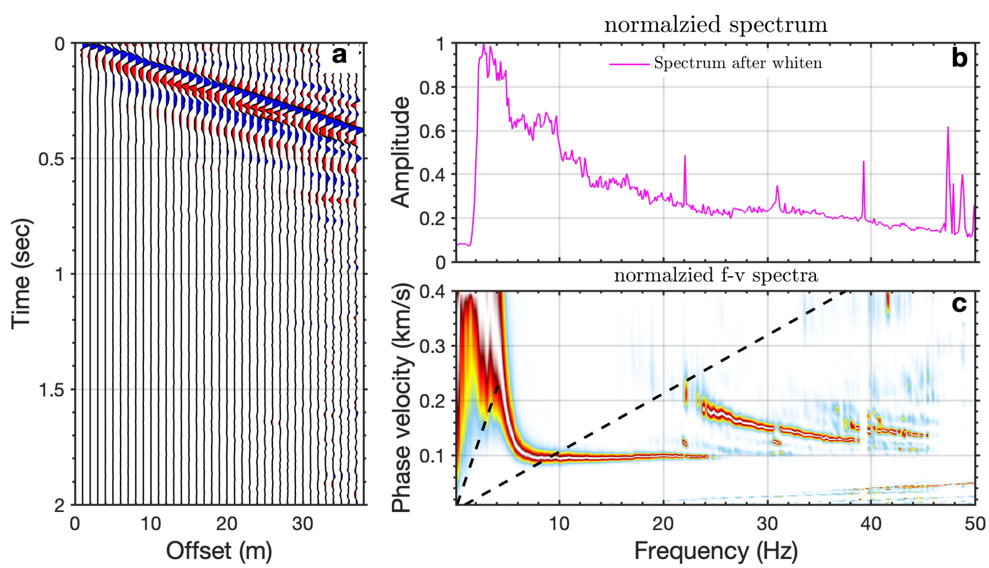

Figure 9: Same as Fig.8 but with spectral whitening included prior to cross-correlation.

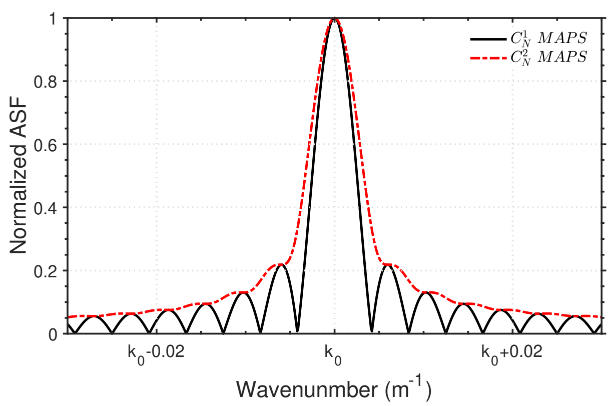

Figure 10: A comparison of ARFs between one virtual-source gather (C_N^1, the black solid line) and multiple virtual-sources gather (C_N^2, the red dashed line). Here we take an array of 24 sensors with 10 m spatial interval as an example.

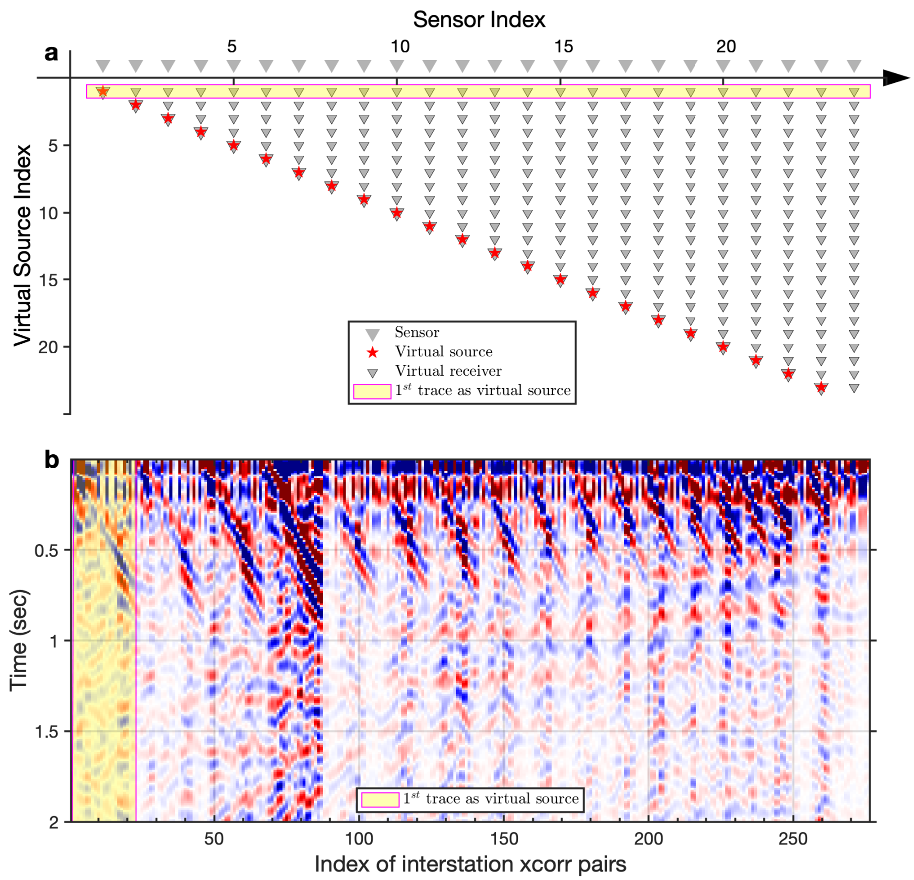

Figure 11: An example of C_N^2 inter-station cross-correlation for field example #2. (a). Virtual source and virtual receiver configuration for C_N^2 inter-station cross-correlation pairs. (b). The extracted C_N^2 inter-station cross-correlation pairs using ambient noise interferometry. The yellow boxes highlight the source and receiver configuration (a) and cross-correlation pairs (b) for one virtual-source gather with the first trace as the virtual source.

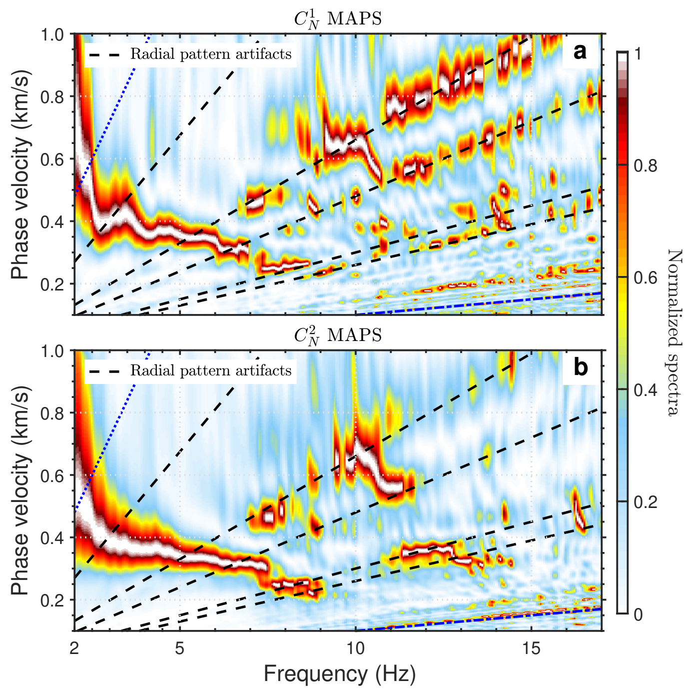

Figure 12: A field example of radial pattern artifacts and their attenuation (modified from Cheng et al. (2019)). (a). Dispersion spectra of MAPS by using the one virtual-source gather. (b). Dispersion spectra of MAPS by using the multiple virtual-sources gather. The black dashed lines indicate the radial pattern artifacts.

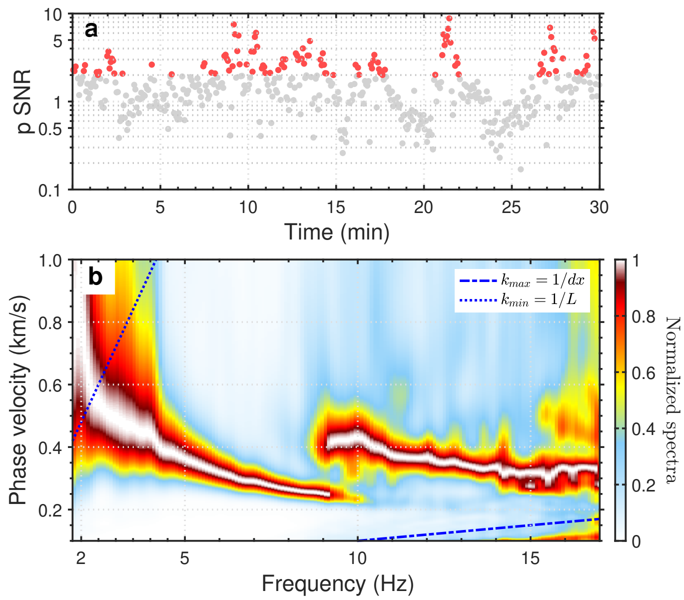

Figure 13: Attenuation of the radial pattern artifacts in Fig.12 using the data-selection technique (modified from Cheng et al. (2019)). (a) displays the estimated SNR indicators using p energy for each time segment during the 30-min observation. The red dotts indicate the selected time segments with p SNR greater than the defined threshold value, 2. (b) shows the enhanced MAPS measurement with radial pattern artifacts significantly attenuated. The blue dotted line indicates the minimum wavenumber reference, and the blue dashed line indicates the maximum wavenumber reference.

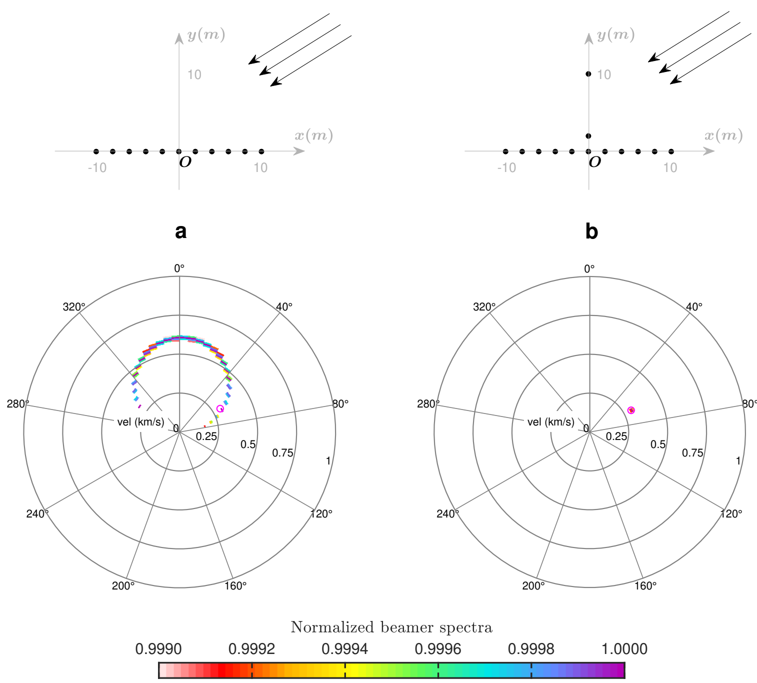

Figure 14: Array responses for the linear array (a) and the pseudo-linear array (b). The black dots denote the receivers; the black arrows indicate the plane wave; the pink circles indicate the target azimuth and velocity solution.

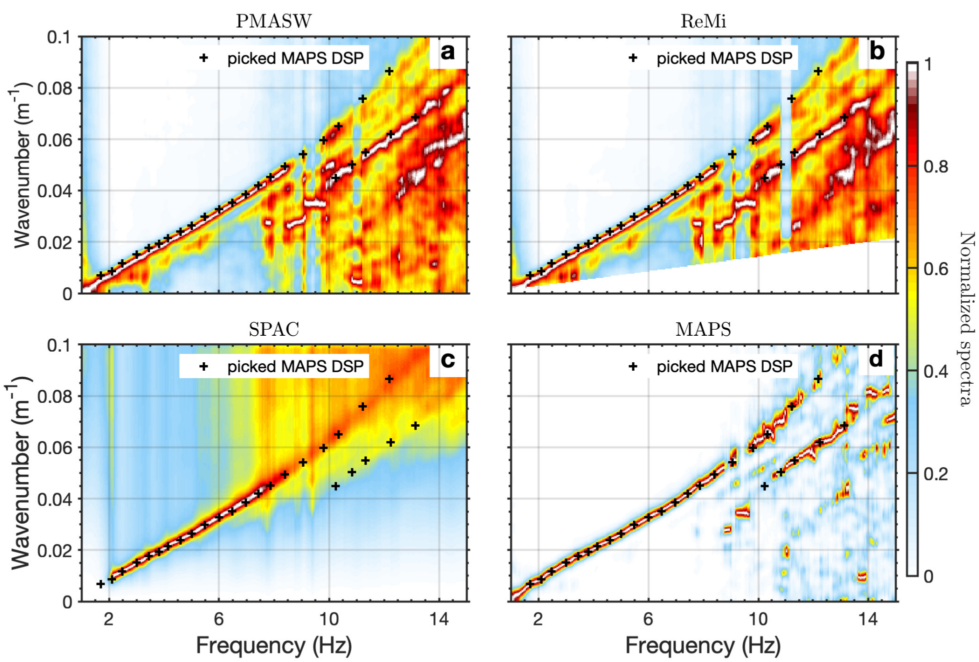

Figure 15: A field example of the artifacts from the non-interferometric methods (modified from Cheng et al. (2020)). (a)-(d) present the obtained dispersion spectra using different passive-source surface wave imaging methods, PMASW, ReMi, SPAC, and MAPS, respectively.